The Development of a Simulator System and Hardware Test Bed for Deep Space X-Ray Navigation

A THESIS

SUBMITTED TO THE FACULTY OF THE GRADUATE SCHOOL

OF THE UNIVERSITY OF MINNESOTA

BY

Patrick T. Doyle

IN PARTIAL FULFILLMENT OF THE REQUIREMENTS

FOR THE DEGREE OF

MASTER OF SCIENCE

Demoz Gebre-Egziabher

September, 2013

Acknowledgements

There are many people I wish to acknowledge that both guided me and contributed to this work, but acknowledging everyone who pointed me in the right direction would be an exercise in futility. Therefore, I apologize for any names that may be excluded henceforth.

First and foremost, I would like to thank my adviser, Dr. Demoz Gebre-Egziabher, without whom I may not have been inspired to pursue the research presented in this thesis. His enthusiasm for teaching and discovery was an inspiration that affirmed my passion for space throughout both my undergraduate and graduate studies.

I would also like to express my sincere gratitude to Dr. Suneel Sheikh, who not only provided invaluable insight into my work, but also became someone I consider a mentor and friend.

There were many others that contributed to this work, notably Curtis Albrecht and Mark Abotossaway, without whom the experiment presented herein would not have flown. Further, I would like to thank Dr. T. Gregory Guzik and the High Altitude Student Platform team from Louisiana State University for providing a means for students to learn about the design and construction of a true engineering project and its associated perils. I also thank NASA's Balloon Program Office for supporting such student-led missions.

I would also like to thank David Chenette, Abraham Kou, and Munther Hindi of

Lockheed Martin Space Systems Company's Advanced Technology Center for providing hardware as well as valuable time, advice, and laboratory support during the development of the payload presented in this thesis. Accordingly, I would like to thank Amptek, Inc. for donating components crucial to the completion of the payload.

I also thank Dr. Darryll Pines and Kevin Anderson of the University of Maryland and Dr. John Hanson of CrossTrac Engineering for their support in the photon simulation studies presented below.

Finally, I would like to thank the Minnesota Space Grant Consortium, especially Dr. James Flaten and Dr. William Garrard for their funding and support in making this research possible.

While I gratefully acknowledge the support from the aforementioned individuals, the views and conclusions contained in this thesis are those of mine alone and should not be interpreted as necessarily representing the official policies, either expressed or implied, of any organization.

Dedication

I dedicate this thesis and its research to my wife, Linnea Marie, without whom I would not have had the love and support I needed to complete my studies.

I would also like to dedicate this work is to my family, especially my parents, Tom and Linda Doyle, for raising me and always encouraging me, and my mother and father-in-law, Pieter and Sherry Maas, for embracing me as one of their own.

Finally, I dedicate this work to my grandfather, the late Captain Ralph Markus, who fostered my love of aerospace and inspired me to pursue my degree through his own passion for aviation, astronomy, and space exploration.

Abstract

Currently, there is a considerable interest in developing technologies that will allow using photon measurements from celestial x-ray sources for deep space navigation. The impetus for this is that many envisioned future space missions will require spacecraft to have autonomous navigation capabilities. For missions close to Earth, Global Navigation Satellite Systems (GNSS) such as GPS are readily available for use, but for missions far from Earth, other alternatives must be provided. While existing systems such as the Deep Space Network (DSN) can be used, latencies associated with servicing a fleet of vehicles may not be compatible with some autonomous operations requiring timely updates of their navigation solution. Because of their somewhat predictable emissions, pulsars are the ideal candidates for x-ray sources that can be used to provide key parameters for navigation. Algorithms and simulation tools that will enable designing and analyzing x-ray navigation concepts are presented. The development of a compact x-ray detector system is pivotal to the eventual deployment of such navigation systems. Therefore, results of a high altitude balloon test to evaluate the design of a compact x-ray detector system are described as well.

Contents

List of Tables

List of Figures

Chapter 1

Introduction

This thesis explores the use of celestial X-ray sources for autonomous deep space navigation and the need to develop small high-energy photon detectors. The term *deep space* can be defined in several ways, one of which is the region of space near or above a *semi-synchronous Earth orbit*, or an orbit about Earth with a period of 12 hours [1]. For the purposes of this thesis, deep space is defined as the region of space near or above a *geosynchronous Earth orbit* (GEO), or an orbit about Earth with a period of 24 hours.

Currently, Global Navigation Satellite Systems (GNSS) such as the United States' Global Positioning System (GPS) provide an inexpensive and accurate way of navigating in *low Earth orbit* (LEO), or orbits up to about 800 km above Earth's surface [1]. However, generation of these global navigation signals requires a large ground and space-based infrastructure. Furthermore, the regular validation and calibration from ground-based stations these global systems require is not readily available in deep space.

Though GNSS can be used in GEO in a limited capacity [2], there are few options that provide autonomous navigation capabilities to spacecraft beyond GEO. X-ray Source-based Navigation for Autonomous Position Determination, or XNAV, is a

possible solution to this shortcoming. XNAV is a concept that uses naturally occurring celestial objects, such as pulsars that emit X-ray signals, as navigation beacons. This technology has the potential to provide navigation autonomy to future deep space vehicles.

1.1 Current Deep Space Navigation Techniques

Current deep space vehicles typically rely on Earth-based radiometric tracking from systems such as NASA's Deep Space Network (DSN) [3]. The large dish antenna DSN facilities are located in California, U.S.A., Madrid, Spain, and Canberra, Australia, and are operated by NASA's Jet Propulsion Laboratory (JPL) in California. The placement of these antennae allow constant 24-hour observation of spacecraft with sufficient overlap to transfer the spacecraft's signal from one complex to another [4]. Radiometric tracking of spacecraft is often enhanced by optical measurements during the approach phase to a target, such as a planet or asteroid, by comparing onboard images to a known star background, but radiometric tracking remains the main navigation technique used on most deep space missions [3].

Deep space radio tracking relies on range measurements and the *Doppler effect*, which causes an observed change in frequency when a transmitter and receiver are moving relative to one another [5], thus providing a means of computing range rate measurements. Spacecraft range, ρ, is measured by the *round-trip light time* (RTLT), τ_{rt}, of a signal generated at one of the DSN stations and transmitted back to Earth by the spacecraft [6], and is approximated by multiplying the RTLT by the speed of light, c, using the expression

$$\rho = \frac{1}{2}\tau_{rt}c. \tag{1.1}$$

Range rate, $\dot{\rho}$, information is approximated using the Doppler effect by

$$f_r = (1 - \frac{\dot{\rho}}{c}) f_t \tag{1.2}$$

where f_r is the frequency of a radio signal received from a spacecraft, and f_t is a known frequency transmitted by the spacecraft [3]. Though Equations 1.1 and 1.2 describe the fundamental physics for determining range and range rate from radio telemetry, the means of accurately obtaining these parameters is much more complex and involves the inclusion of error sources such as spacecraft clock instability, transmission media, antenna location on Earth's surface, and Earth orientation parameters as described in [3].

The DSN is a proven system that provides accurate navigation solutions to deep space vehicles. However, even though the DSN radio signals required for navigation and communication travel at the speed of light, they have inherent time delay when relaying signals between the Earth and deep space vehicles [3, 6]. For instance, a spacecraft such as NASA's Voyager 1 currently operating near the boundary of interstellar space (about 18 billion kilometers distant from the Sun) requires communication times on the order of about 34 hours to send and receive a signal from Earth. Although the DSN provides high accuracy ranging along the line of sight between Earth and a spacecraft (Doppler error on the order of mm/s) [3], the delay in sending a signal between a deep space vehicle and Earth would inhibit a constellation of smaller satellites performing cooperative scientific objectives that require fast updates of the navigation solution. Thus, an autonomous navigation system will allow a spacecraft to perform the necessary guidance and control actions to achieve its scientific objectives without the need of persistent communication with Earth.

1.2 Current and Future Deep Space Missions

Many envisioned deep space missions, such as long-range sample return or planetary monitoring constellations, will require spacecraft to have autonomous navigation capabilities in order for the spacecraft to operate without continuous contact form Earth-based stations. There are also current deep space missions that would benefit from increased autonomy, which would relieve demands on Earth-based systems such as the DSN.

NASA's New Horizons spacecraft is the first man-made vehicle with a primary scientific objective of exploring the dwarf planet Pluto and its moon Charon [7, 8]. Though the spacecraft is placed in a *hibernation mode* with Earth-based updates taking place annually throughout most of the cruise portion of its flight, such a vehicle could benefit from autonomous navigation capabilities. With a functional XNAV system, the vehicle could make real-time corrections to its trajectory throughout its journey and navigate on its own to Pluto without annual communications from Earth. Upon commencement of its primary scientific objectives, the spacecraft could utilize XNAV to adjust its trajectory within the Pluto-Charon system rapidly, thus making scientific observations quickly while relying on the DSN for transmission of its collected data rather than consuming bandwidth to perform trajectory updates and vehicle attitude corrections. Although XNAV would currently be considered a redundant system on a vehicle such as New Horizons due to its reliance upon the DSN, there are several scenarios in which XNAV would be indispensable.

Currently, several manmade vehicles are operating at Mars. These vehicles include NASA's Curiosity and Opportunity rovers, NASA's Mars Odyssey and Mars Reconnaissance Orbiter (MRO) spacecraft, and the European Space Agency's (ESA) Mars Express spacecraft. The current orbiters operating at Mars serve as a communications bridge between Earth and Mars [9]. Thus, along with their primary scientific objectives,

these spacecraft also relay information to and from the rovers on Mars' surface.

The implementation of a fleet of XNAV-capable spacecraft in Martian orbit would be invaluable to future missions to Mars, including the anticipated human exploration of the Martian surface. Such a fleet of spacecraft would be able to navigate relative to a vehicle serving as a communications hub between Earth and Mars. A communications spacecraft equipped with a large X-ray detector could provide updates to a fleet of smaller vehicles equipped with smaller, less expensive detectors that may receive only a portion of the navigation signal described in the following section. These smaller vehicles could serve as communication relays for humans not in direct contact with the Earth-Mars communications hub. The smaller remote spacecraft would be less expensive and would not require the DSN to be in direct contact with them to perform necessary trajectory corrections. This scenario would allow humans to have a constant Earth-Mars connection without the need for an expensive Mars-based radio antenna system such as the DSN.

There is also current interest in establishing a permanent human presence on the moon. A lunar satellite network, such as that described for Mars, with a communications hub operating at one of the Earth-Moon *Lagrange points*, such as the L1 point, would allow human explorers to be in constant contact with Earth anywhere on the lunar surface. Thus, XNAV has the potential to be essential to humanity's inevitable presence in deep space. Such XNAV-based satellite networks will ensure that there is always a link home without the need to construct expensive ground-based communications infrastructure at remote outposts.

1.3 The Use of Natural Celestial X-Ray Sources as Navigation Beacons

Recent work has shown that celestial X-ray sources such as pulsars can be used as navigation beacons for determining the absolute and relative position of space vehicles [10–22]. Such sources naturally occur at vast astronomical distances and do not require any Earth-based operations to utilize them as beacons. Though many space vehicles use celestial-based systems such as star trackers and sun sensors to provide a portion of their navigation solution, they still rely significantly on Earth-based operations. X-ray pulsars, however, are capable of providing a signal that can be used for a fully autonomous navigation system. The Defense Advanced Research Program Agency (DARPA) and NASA program names for this concept is known as X-ray Source-based Navigation for Autonomous Position Determination, or XNAV.

A pulsar is a rapidly rotating neutron star that emits a beam of electromagnetic radiation along its magnetic field axis [23, 24]. The magnetic axis is often offset from the axis of rotation, thus the star appears to emit pulses of radiation as the magnetic poles sweep past an observer. A simple analogy for a pulsar is a lighthouse on Earth's seashores. As the lighthouse's beacon rotates, a ship at sea views bright flashes of light and safely navigates along the shore. Similarly, as a pulsar rotates, a spacecraft will view bright flashes of electromagnetic radiation and navigate along its trajectory. A schematic drawing that illustrates this principle is shown in Figure 1.1 below. An observer aligned along the path of the magnetic axis will encounter these periodic flashes.

Pulsars are excellent candidates for use as X-ray navigation beacons. This is because their signals can be used to support time determination at a spacecraft and to provide range and range-rate measurements – key parameters for position determination. It has been demonstrated that the stability of pulsar spin rates compares well to atomic clocks

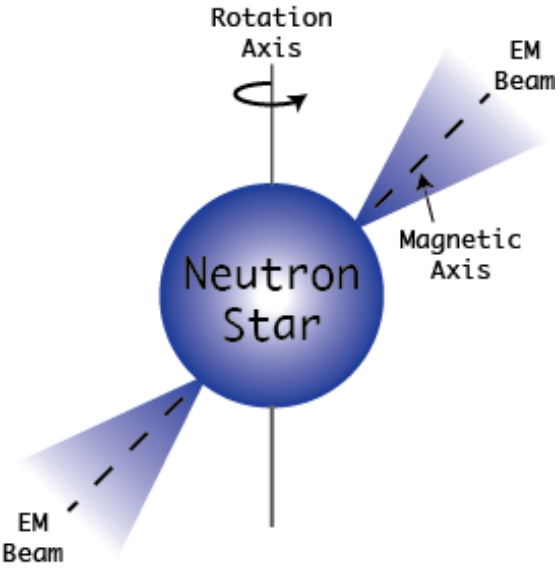

Figure 1.1: Illustration of a typical pulsar showing its electromagnetic (EM) beams with the magnetic axis offset from the rotation axis.

(with fractional stabilities on the order of 10^{-14} over durations of days to months) [25]. Furthermore, X-ray signals from pulsars have identifying signatures [23, 24]. However, because the distance to even the closest pulsar is on the order of kilo-parsecs (thousands of light years distant) and signal losses occur due to absorption and dispersion, the *signal-to-noise ratio* (SNR) of the received X-ray signals is small. Current methods for detection of these low SNR signals rely on counting a number of individually detected photons in some known time interval. Measuring the energy level of a detected photon also provides information that helps categorize the photon as an X-ray or other cosmic ray, such as a gamma ray, thus allowing higher energy particles to be excluded from X-ray navigation algorithms.

These detection methods record specific peaks by accumulating sufficient photons and synchronously averaging these photons based upon a pulsar's measured pulse frequency, thus allowing the source pulsar's pulse *time-of-arrival* (TOA), as well as pulse shape, to be identified. This process of synchronous averaging is known as *folding*, and

is used to improve the SNR of the detected pulse through the addition of many pulses so that the signal is visible above the background noise [23, 26]. The folding process is described in detail in Chapter 3. Since most X-ray pulsars have faint signals at Earth, this implies that accurate pulse phase measurements require large X-ray detector areas, long signal collection times, or both. Simulated pulse profiles from the two pulsars PSR B1821-24 and PSR B1937+21 are presented in Figure 1.2 below.

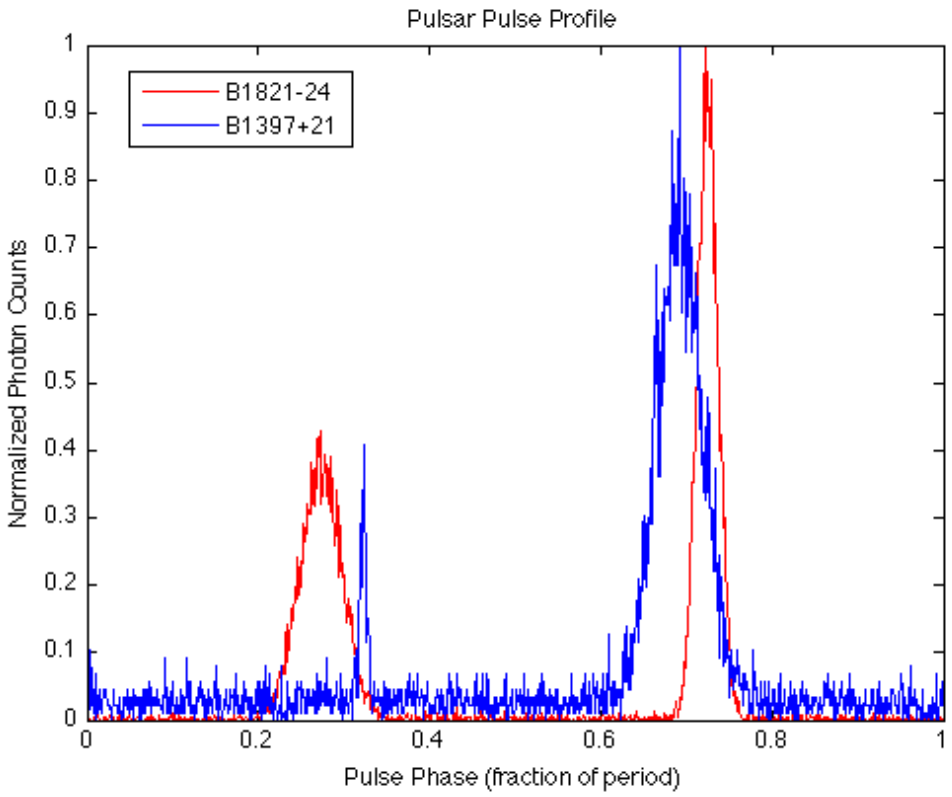

Figure 1.2: Simulated pulse profiles for pulsars B1821-24 (red) and B1937+24 (blue). The pulses are plotted as normalized photon counts that have been binned and folded over the pulsars known period.

As seen by the examples in Figure 1.2, each pulsar has a unique pulse profile. Due to their particular evolutions, each pulsar has a distinctive period that is well known

or can be modeled. The periods for these two pulsars are on the order of milliseconds; B1821-24 is 0.00305 s [27], while B1937+21 is 0.00155 s [28]. Thus after several minutes of collection time, hundreds of thousands of these pulses would register on a capable X-ray detector. The pulse profiles in Figure 1.2 are plotted by using a series of simulated photon time events generated over several thousand seconds for each source. These events are then folded into smaller bins as fractions of the whole period of each source pulsar, thus allowing each pulsar to be plotted on the pulse phase, or period fraction, scale as described in Chapter 3. These signals are well known and understood, thus any signal received at a detector on a spacecraft can be compared to a database of known pulsars such as B1821-24 and B1937+21.

In addition to pulsars it has been demonstrated that aperiodic X-ray sources can be used to obtain a *relative navigation* solution in which several spacecraft operating cooperatively need to navigate with respect to one another instead of with respect to an *inertial frame of reference* [15, 16]. Such sources do not necessarily exhibit the same periodic behavior as pulsars, but through cross-correlation, a relative navigation solution can be extracted from such a source.

It has been demonstrated that detectors with areas larger than 1 m^2 provide position accuracies using X-ray pulsars that are acceptable for many space-based applications [11, 13–16]. While detectors of this size can be used on larger space vehicles, they are impractical for smaller ones. Further, it has not been demonstrated that proposed small detectors [29] provide such accuracies on long-term flights. Such detectors have areas on the order of tens of square centimeters rather than square meters, and can be placed on any number of deep space vehicles.

Current XNAV techniques are applicable to many deep space operations where GNSS signals are not available or DSN tracking is not possible, such as due to reduced accuracy when a spacecraft is very far from Earth or when it is operating behind

a planet [30, 31]. While the current demonstrated accuracy of XNAV is not at the level of GNSS [11, 13], XNAV is a nascent technology and it is reasonable to expect future increases in its accuracy. This increased performance will be the result of future improvements in high-energy photon sensors, as well as photon processing and navigation algorithms.

1.4 Problem Statement

The work described in this thesis is an effort to address the relatively unknown performance of small X-ray detectors on separate, cooperating spacecraft. One approach to mitigate this challenge is to develop algorithms to generate accurate navigation solutions using small detectors that provide relative range measurements in spite of the low SNR. This is aided by developing a simulator to produce simulated photons over a very long duration using a modeled small detector, while maintaining proper accounting of the relative motion as the spacecraft translates along its trajectory. The ability to make precise time measurements on photons detected by a small detector is imperative because the measurements are scaled by the speed of light, c (about 3×10^8 m/s). This implies that timing errors on the order of 10 microseconds (10×10^{-6} s) translate to a position error on the order of 3 km. Thus for precision navigation, relativistic effects that provide timing errors on the order of nanoseconds (1×10^{-9} s) must be taken into account while modeling a celestial X-ray signal.

Detector hardware must also be built and flown in order to effectively model a noise-corrupted pulsar signal as received by a moving small detector. Once such detectors have some proven flight history, then their performance characteristics will be better understood, thus allowing models for these small detectors to be improved. Therefore, a test bed designed for flight at high altitudes can be used to test photon sensor upgrades as well as perform analysis on improvements to photon processing and navigation

algorithms.

1.5 Thesis Contribution

In view of the challenges mentioned above, this thesis contributes the following:

- XNAV algorithms (akin to carrier phase differential GNSS [2, 32]) for small and compact X-ray detectors to generate an accurate navigation solution.
- The X-Ray Photon and Relativistic Effect Simulator System (XPRESS), a simulator capable of modeling a pulsar's signal at a small detector on a moving spacecraft.
- The High Altitude X-Ray Detector Testbed (HAXDT), a hardware system built to fly on a high-altitude scientific balloon and test small detector designs.

1.6 Thesis Organization

- Chapter 2 provides an overview of X-ray navigation concepts and how such systems and algorithms might work.
- Chapter 3 describes the mathematical models used in the development of a system capable of simulating celestial X-ray sources and presents algorithms and analysis on the simulation of precise photon time events.
- Chapter 4 describes the development of a high-altitude test bed to test X-ray detector hardware and avionics systems and outlines results obtained from a flight on a high-altitude scientific balloon.
- Chapter 5 presents a conclusion on the analyses presented in this thesis and outlines future work.

Chapter 2

X-Ray Navigation Concepts

There are several operational concepts currently being investigated in which XNAV is the primary navigation technique. These concepts include both *absolute* and *relative* position determination of deep space vehicles [15, 16, 20]. In the absolute scenario, a spacecraft navigates with respect to some inertial frame of reference, while in the relative scenario, a spacecraft navigates with respect to some other non-inertial, or moving frame of reference such as another spacecraft translating along its own trajectory.

The *Solar System barycenter* (SSB), or the center of mass of the solar system, serves as an inertial frame of reference for timing of celestial X-ray source signals [23, 24]. Timing models for celestial X-ray sources are constructed at the SSB based on astrophysical observations, thus the SSB serves as an inertial frame of reference upon which received signals at a spacecraft are transferred and compared to the known model. Both absolute and relative navigation are pictured schematically in Figure 2.1 below, where a space vehicle with a large X-ray detector (a Mother ship) works cooperatively with a number of vehicles with smaller detectors (Daughter ships) to generate a relative navigation solution – the position of the Daughter ships relative to the Mother ship – referred to as the Mother-Daughter scenario.

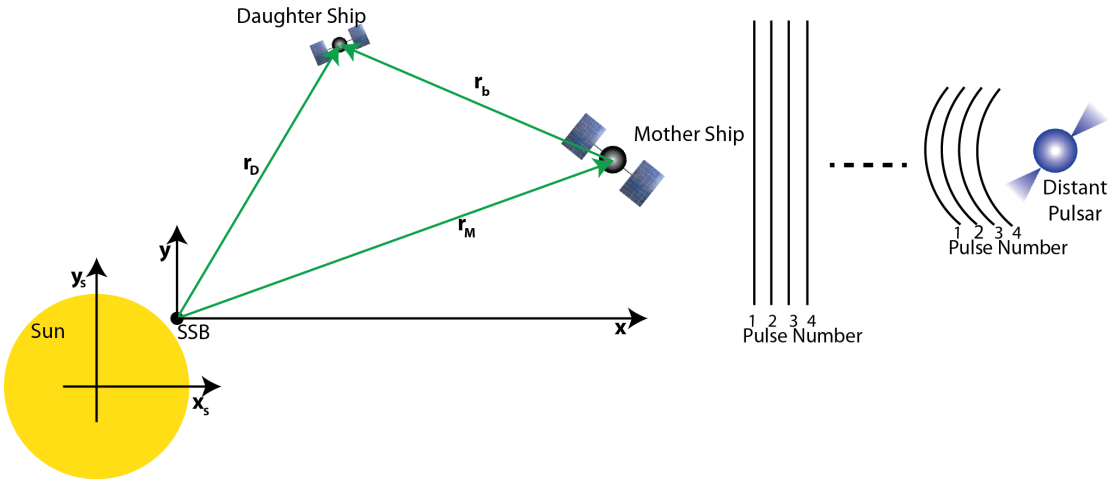

Figure 2.1: The Mother-Daughter navigation scenario in which a Daughter ship navigates relative to a Mother ship. Pulses from a distant pulsar arrive in the solar system as planar waves.

As illustrated by Figure 2.1, the absolute navigation problem is that of determining the Mother ship's position with respect to the SSB, $\mathbf{r_M}$, while the relative navigation problem is that of determining the baseline vector, $\mathbf{r_b}$. If the absolute position of the Mother ship is known, then the absolute position of the Daughter ship, $\mathbf{r_D}$, can be computed by taking the vector difference between $\mathbf{r_M}$ and $\mathbf{r_b}$. Due to the vast interstellar distances that pulsar signals travel through it can be assumed that the pulses arrive as planar wave fronts as shown in Figure 2.1. The remaining sections of this chapter include a brief outline of absolute position determination using X-ray pulsars and proposed algorithms for the Mother-Daughter relative X-ray navigation scenario.

2.1 Absolute Navigation of Deep Space Vehicles Using X-ray Pulsars

The ability of a spacecraft to determine its absolute position is essential to autonomous navigation. Such a system can operate without assistance from external sources such as GPS or the DSN. This capability would make the spacecraft able to determine it's position in even the most extreme case of the spacecraft being lost in space.

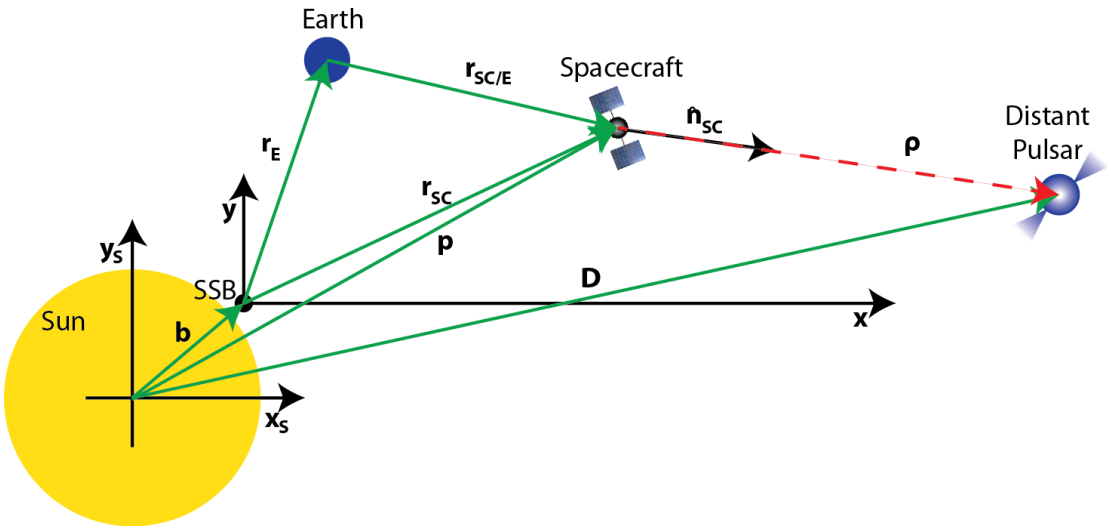

Figure 2.2: Geometry of a spacecraft navigating with respect to the SSB, $\mathbf{r_{sc}}$.

Pulsar signals, such as those shown in Figure 1.2, arriving at a detector onboard a spacecraft can be described as some integer number of such pulses, N, plus some fraction of one of these pulses along the line of sight vector to the source pulsar, $\hat{\mathbf{n}}_{\mathbf{sc}}$. A two-dimensional representation of a spacecraft navigating using a pulsar is shown in Figure 2.2. The spacecraft's range, ρ, to the pulsar can be computed using the time the signal is transmitted at the source pulsar, t_T, and the time the signal is received at a

detector on a spacecraft, $t_{R_{sc}}$ by the following [15],

$$\rho = c(t_{R_{sc}} - t_T) = \hat{\mathbf{n}}_{sc} \cdot (\mathbf{D} - \mathbf{p}) + RelEff \tag{2.1}$$

where $\mathbf{D}$ is the position of the source pulsar with respect to the sun and $\mathbf{p}$ is the position of the spacecraft with respect to the sun as shown in Figure 2.2. The term *RelEff* refers to higher order relativistic effects, which are explored in Chapter 3 where signal modeling is discussed in further detail. As indicated by Equation 2.1, if the transmit and receive times of an individual pulse are known, then the range measurement, ρ, can easily be computed. However, because celestial sources do not provide a means of determining the pulse transmission time, t_T, the range cannot be directly computed using Equation 2.1 [15].

Absolute position determination using pulsars requires the identification of which specific pulse is being detected at a certain time, but pulsars do not provide any means of identifying individual pulses [15]. Therefore, by comparing pulse timing models at a known location, such as the SSB, then it is possible to determine a set of phase differences in the detected pulse and the model at the SSB. Such differences can remove terms that cannot be measured directly, such as pulsar distance, and are similar to differences computed in GPS integer ambiguity resolution [2, 32]. The description of these methods is outside the scope of this thesis, so the interested reader is referred to [15].

2.2 Algorithm Development for the Mother-Daughter Relative X-ray Navigation Scenario

In view of the challenges associated with small area X-ray detectors, this thesis proposes that relative XNAV algorithms (akin to carrier phase differential GNSS [32]) can be used. Such navigation techniques will allow improved navigation accuracies when using X-ray

detectors with small effective collection areas. In the relative XNAV approach proposed here, a space vehicle with a large detector (a Mother ship) will work cooperatively with a number of vehicles with smaller detectors (Daughter ships) to generate a relative navigation solution, previously referred to as the Mother-Daughter scenario. If the absolute position of the Mother ship is known (e.g., for lunar missions it can be parked at one of the Earth-Moon Lagrange points) then the absolute position of the Daughter ships can be determined. Of course, in some instances only the relative navigation solution may be what is needed and, thus, the absolute position of the Mother ship need not be known.

2.2.1 Theory and Equations

The basic idea behind relative X-ray navigation is shown in Figure 2.3. A pulsed X-ray signal from a distant pulsar arrives at a detector onboard a spacecraft. Since the distance between the pulsar and the detector is large, it is assumed that the pulses arrive at the detector as planar waves as shown in Figure 2.1. Such pulses have distinct peaks after correctly folding the collected photons and accounting for all geometric and relativistic effects. Thus, a bin with a maximum number of photons in some known time interval or a maximum energy released by the photons as registered on a detector can form the basic navigation measurement. This maximum bin can then be associated with the pulse TOA. Due to the periodic nature of the source pulsar, this measurement will be analogous (algorithmically) to a radio frequency carrier wave. These signals have a signature wavelength, λ, with corresponding fiducial peaks. Therefore, for the discussion that follows we assume the largest fiducial peaks signal the start of the waveform.

A Mother-Daughter pair of space vehicles is shown in Figure 2.3 where the SSB is used as the origin of the navigation frame. The signal from a distant pulsar arrives at the two spacecraft that are separated by the baseline vector $\mathbf{r_b}$. Due to the large

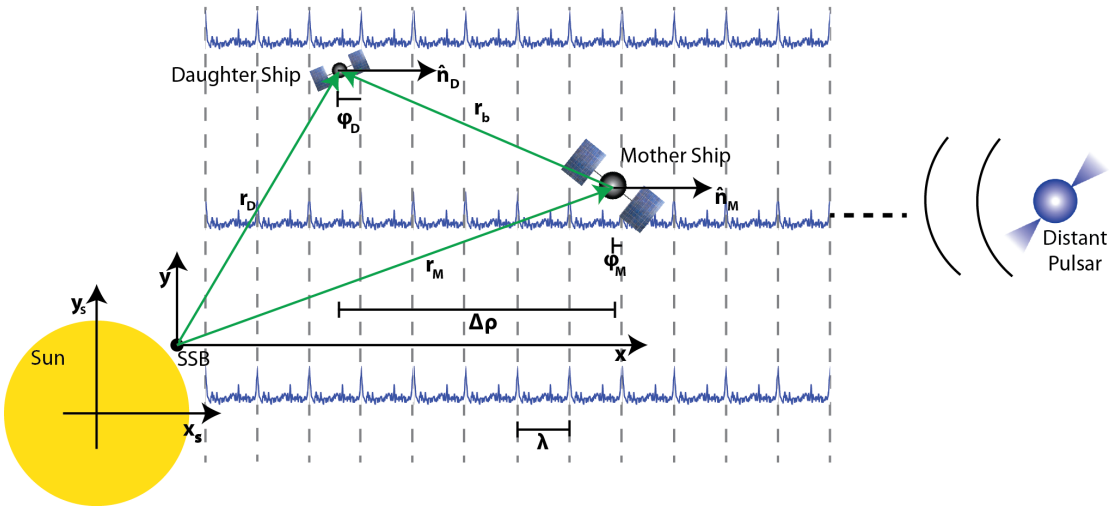

Figure 2.3: A Mother ship and Daughter ship spacecraft are able to determine their relative position, $\mathbf{r_b}$, using X-ray signals along the line of sight vector, $\hat{\mathbf{n}}$, from a distant pulsar.

distance between the vehicles and pulsar along with the close proximity in which the vehicles are operating, it is assumed that the line-of-sight vectors from the Mother and Daughter ships to the pulsar are parallel. These vectors (which are unit vectors) are denoted as, $\hat{\mathbf{n}}_M$ and $\hat{\mathbf{n}}_D$ respectively in Figure 2.3. Since these unit vectors are parallel they are also equal, and for simplicity they will be denoted as $\hat{\mathbf{n}}$. This condition also holds for the unit vector to the source pulsar from the SSB, $\hat{\mathbf{n}}_{SSB}$ (not illustrated in Figure 2.3), thus all unit vectors in the navigation scenario are equal to the unit vector of the astrophysical barycentric model of the celestial source, or $\hat{\mathbf{n}}_M = \hat{\mathbf{n}}_D = \hat{\mathbf{n}}_{SSB} = \hat{\mathbf{n}}$.

The position vector of the Daughter ship relative to the Mother ship as shown in Figure 2.3 is the baseline vector, $\mathbf{r_b}$. The baseline and unit vector to the source have the components:

$$\mathbf{r_b} = \begin{bmatrix} \Delta x & \Delta y & \Delta z \end{bmatrix}^T \tag{2.2}$$

$$\hat{\mathbf{n}} = \begin{bmatrix} n_x & n_y & n_z \end{bmatrix}^T \tag{2.3}$$

where Δx, Δy, and Δz are the three-dimensional differences in position between the Daughter and Mother ships.

We begin to relate the relative navigation solution, or baseline $\mathbf{r_b}$, to the signals received from the pulsars by denoting the range of each spacecraft from the SSB towards the pulsar as, ρ_M and ρ_D for the Mother and Daughter vehicle, respectively. These range measurements at some time, t_0, can be described as a fraction of the pulsar's signal wavelength, $\phi(t)$, plus some integer number of wavelengths as follows:

$$\rho_M = \lambda[\phi_M(t_0) + N_M(t_0)], \tag{2.4}$$

$$\rho_D = \lambda[\phi_D(t_0) + N_D(t_0)], \tag{2.5}$$

where λ is the wavelength of the signal, N_M and N_D are the integer number of wavelengths to the source pulsar, and ϕ_M and ϕ_D are the fractional position of the Mother and Daughter ships within one pulse's wavelength as shown in Figure 2.3. The difference in the range between the two spacecraft, $\Delta\rho$, along the line of sight to the pulsar is the projection of $\mathbf{r_b}$ onto $\hat{\mathbf{n}}$, and is therefore the scalar product between the two vectors. The difference $\Delta\rho$ then expands to:

$$\begin{aligned} \Delta\rho &= \rho_D - \rho_M \\ &= \hat{\mathbf{n}} \cdot \mathbf{r_b} \\ &= n_x\Delta x + n_y\Delta y + n_z\Delta z \\ &= \lambda[\phi_D(t_0) - \phi_M(t_0) + N_D(t_0) - N_M(t_0)] \\ &= \lambda(\Delta\phi + \Delta N) \end{aligned} \tag{2.6}$$

This relationship can be rearranged for any integer number of pulsars, $k \geq 1$ as follows:

$$\begin{bmatrix} \lambda_1 \Delta\phi_1 \\ \lambda_2 \Delta\phi_2 \\ \vdots \\ \lambda_k \Delta\phi_k \end{bmatrix} = \begin{bmatrix} n_{x_1} & n_{y_1} & n_{x_1} \\ n_{x_2} & n_{y_2} & n_{x_2} \\ \vdots & \vdots & \vdots \\ n_{x_k} & n_{y_k} & n_{x_k} \end{bmatrix} \begin{bmatrix} \Delta x \\ \Delta y \\ \Delta z \end{bmatrix} \Rightarrow \mathbf{\Phi} = \mathbf{G}\mathbf{r_b} - \mathbf{\Delta N} \tag{2.7}$$

This is the relative XNAV equation and it turns out to be identical to the carrier phase differential GNSS equation where $\mathbf{\Phi}$ is the vector of observables, $\mathbf{G}$ is the geometry matrix, $\mathbf{r_b}$ is the baseline vector and $\mathbf{\Delta N}$ is composed of the single difference integer ambiguities [33]. Note that in Equation 2.7, there are then k-equations with more unknown variables than equations as both $\mathbf{r_b}$ and $\mathbf{\Delta N}$ are unknown. To extract the relative navigation solution we must first solve for the integer ambiguities. This is well studied in GNSS literature and there are many robust algorithms for solving it, notably LAMBDA [33]. Thus, in theory this problem can be easily solved [11, 15].

2.2.2 Challenges

While the structure of the relative XNAV and carrier phase differential GNSS equations is the same, the observables in the vector $\mathbf{\Phi}$ and the measurement errors are very different. This difference makes extending algorithms such as LAMBDA to relative XNAV problematic. There are at least three significant differences that must be addressed before Equation 2.7 can be used in a relative XNAV solution.

1. GNSS signals are well understood and carry transmission time information [2, 32], whereas an accurate description of pulsar signals is that they are non-homogeneous Poisson stochastic processes. Given a large detector and a sufficiently long observation time, a time series model of the signal can be developed. However, with

a small detector, the background photon flux may overwhelm the pulsar signal such that it may not be possible to construct a complete picture of the time series of the received photon history. Thus, the observables at the Daughter ship will have to be synthetically created by correlating or fusing the observables from the Mother ship with the low SNR signal of the Daughter. It is not clear what the impact of this will be on the relative XNAV problem as represented by Equation 2.7.

2. There are operational aspects of the relative XNAV problem that are different from GNSS. For example, it is not clear what the effect of pulsar geometry will be on the quality of the solution generated. It is also a challenge to make multiple measurements of different pulsars with one detector and track the separate signals as the spacecraft moves along its trajectory. Thus, if case studies of specific lunar operations are performed, will there be enough pulsars in view to receive a sufficient number of signals that will allow solving Equation 2.7, and how many detectors would be needed to track these pulsars? Additionally, what are the data communication bandwidth requirements and how do they fit into power budgets and communication budgets of small spacecraft?

3. An assumption built into the differential GNSS algorithms is that the observables received from the transmitter are time-stamped and, thus, the Mother and Daughter detector measurements can be synchronized. This is not the case with relative XNAV because pulsar signals are neither deterministic nor are they generated by a transmitter like GNSS signals. Therefore, timing errors (δt, akin to clock errors in GNSS) must be modeled or accounted for in the solution. In addition, there are other relativistic errors in pulsar ranging that do not have a good analog in GNSS, so their effect on Equation 2.7 needs to be studied [11, 14, 22, 34].

2.3 XNAV Contribution

In view of the challenges mentioned above, it is clear that a simulator capable of modeling a pulsar's signal at a small detector onboard a moving spacecraft must be implemented in order to effectively test XNAV algorithms. Further, detector hardware must be built and flown in order to effectively model a noise-corrupted pulsar signal as received by a moving small detector. Once these detectors have some proven flight history, then their performance characteristics will be better understood, thus allowing models for these small detectors to be improved. Thus, the remainder of the work presented in this thesis addresses these specific needs.

Chapter 3

X-Ray Photon and Relativistic Effect Simulator System

In order to effectively test XNAV algorithms such as those presented in Chapter 2, a simulator capable of modeling a pulsar's signal at a small detector on a moving spacecraft must be developed. The ability to make precise time measurements on detected photons is critical because the measurements are scaled by the speed of light, c. This scaling implies that timing errors on the order of 10 μs translate to a position error on the order of 3 km, so for precision navigation, timing error precision on the order of 10 ns is required for meter-level position errors. This means that relativistic timing errors need to be included in addition to geometric effects. Therefore, in cooperation with ASTER Labs, Inc., CrossTrac Engineering, Inc., Microcosm, Inc., and the University of Maryland, the X-Ray Photon and Relativistic Effect Simulator System (XPRESS) has been developed to fill the need for a tool capable of modeling X-ray photons.

3.1 XPRESS Overview

XPRESS is a Matlab simulation system designed to assist analysis and algorithm verification of X-ray based systems such as X-ray navigation, timing, and attitude determination. This tool generates random X-ray photons based upon user-defined input parameters. These inputs include detector, source, and celestial background attributes as well as spacecraft dynamics and simulation parameters. The inputs reside in data header files, which are pre-processed to extract all relevant data used in the simulation. At the heart of the XPRESS code is a random photon generator developed by CrossTrac Engineering, Inc. [35]. The generator utilizes non-homogeneous Poisson processes to generate random barycentric photon time events. These photon time events then go through a series of processing routines, including the incorporation of spacecraft dynamics and folding the photon events to extract the pulse profile. Finally, XPRESS provides a series of outputs including the barycentric event times along with spacecraft *uncorrected* and *corrected* event times. The folding process is described in Section 3.1.1, while the uncorrection and correction process is described in Section 3.1.2. Figure 3.1 below shows the XPRESS processing flow diagram as well as a summary of the attributes and parameters defined in the data header files.

Built into XPRESS are six different modes with varying degrees of accuracy that simulate various combinations of the geometric and relativistic delay terms used in the uncorrection and correction process. These modes and their associated time transfer equations are described in detail in Section 3.2. The purpose of having several different modes is to provide users with the option of ignoring relativistic delay terms in order to speed up processing time and test algorithms quickly. Once algorithms are developed, then XPRESS can assist in their verification by providing a detailed simulation of an X-ray source. For the purpose of this thesis, X-ray pulsars have been modeled and the results analyzed to assist in efforts to develop XNAV systems. There have also been

efforts to simulate an aperiodic X-ray source in an attempt to expand the system's capabilities, but the results of these efforts will be the product of future XPRESS upgrades.

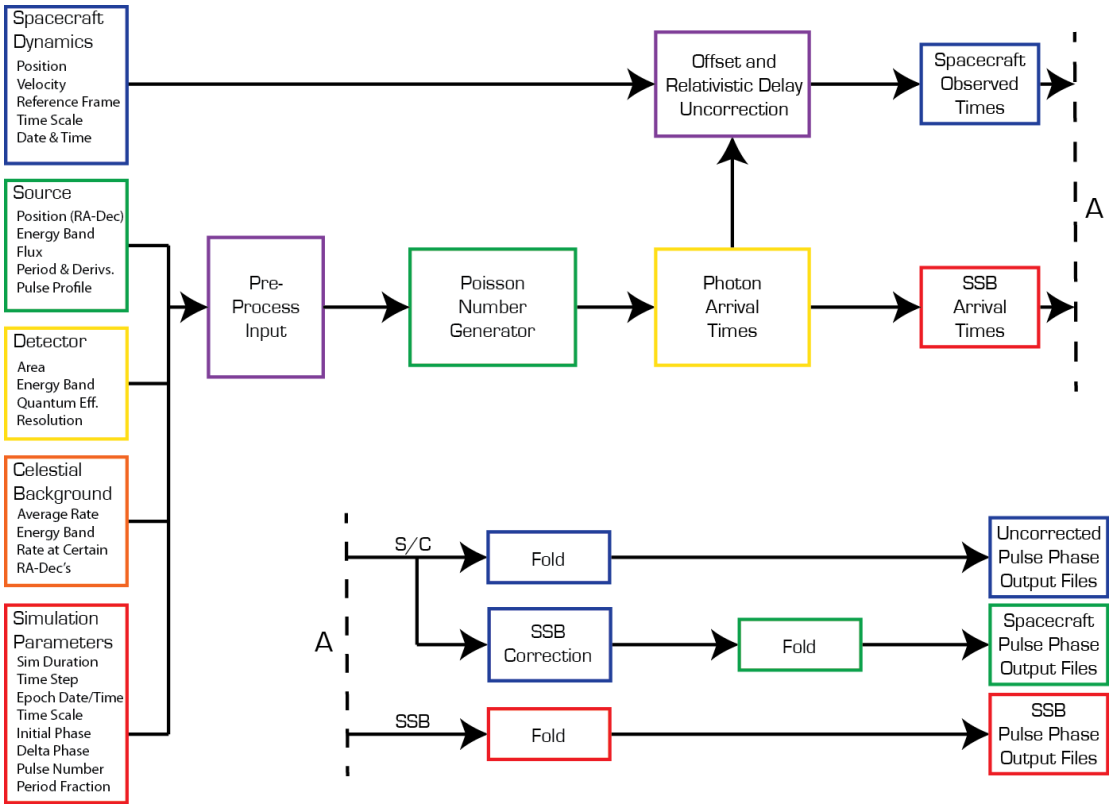

Figure 3.1: XPRESS processing flow diagram showing user-defined inputs and the resulting outputs from the simulation.

3.1.1 Folding

Folding is a type of synchronous averaging that is used to extract a source pulsar's pulse TOA and pulse shape, or profile. This process of synchronous averaging is used to improve the SNR of the detected pulse through the addition of many pulses so that the signal is visible above the background noise [23, 26]. Folding is based upon a pulsar's

measured period and requires the collection of X-ray photons over many of the source pulsar's periods. The folding algorithm used in XPRESS is similar to that presented in [23], and is summarized as follows:

1. Create an array for storing the folded pulse profile separated into a number, n, of equally spaced elements across the pulsar's period called bins, thus creating an array of bins that each correspond to a particular phase of the pulse period.

2. Calculate the phase of a photon time event relative to the pulse period, which involves taking the modulus of the photon time event over the pulse period.

3. Add the photon time event to the bin corresponding to the nearest phase.

4. Repeat the process for all photon time events.

The algorithm described above results in a pulse profile, such as those shown in Figure 1.2, that represents the average emission from a source pulsar over the pulsar's rotational period.

3.1.2 Uncorrection and Correction

The process of uncorrecting and correcting photon time events serves as a verification that the delay terms have successfully been applied to the barycentric photon event times generated by XPRESS, thus ensuring the proper simulation of photon time events at a detector on a moving spacecraft. The term *uncorrected* is used to describe photon events detected by a spacecraft at some time, t_{SC}. These events occur in a translating frame of reference due to vehicle dynamics that must be transferred to an inertial frame of reference, or the SSB, in order to compare the measured events to the astrophysical timing model at the SSB. The term *corrected* is used to describe photon events that have had geometric and relativistic effects added to the spacecraft time events in order

to transfer the time events back to the SSB, t_{SSB}, as shown in Equation 3.2 below. The $Delay\ Terms$ indicated in the two equations are described in detail in Section 3.2.

$$t_{SC} = t_{SSB} - Delay\ Terms \tag{3.1}$$

$$t_{SSB} = t_{SC} + Delay\ Terms \tag{3.2}$$

Several steps must be taken to implement the uncorrection and correction process. First, it must be verified that the spacecraft's trajectory is known prior to the first barycentric arrival time so that the uncorrection in Equation 3.1 can be performed. Next, it must be determined which SSB time event matches the same time event detected at the spacecraft in order to return the proper uncorrected spacecraft time event. Finally, the uncorrected spacecraft time events must be corrected back to the SSB (Equation 3.2) and checked for errors. The algorithm used to perform the uncorrection and correction is as follows:

1. XPRESS photon generator simulates the t_{SSB} photon time events.

2. A test spacecraft time event, $t_{SC_{test}}$, is computed for the first barycentric time event, t_{SSB_1}.

3. The simulation terminates and reports an error if $t_{SC_{test}}$ is greater than the spacecraft trajectory start time, thus ensuring the trajectory is known prior to the barycentric arrival.

4. Each barycentric time event undergoes an iteration routine whereby the barycentric event, t_{SSB}, is aligned with a spacecraft position and uncorrected to return t_{SC}. This subroutine is as follows:

   (a) An estimated uncorrected time event is assigned such that $t_{estimate} = t_{SC_{test}}$.

(b) The spacecraft's trajectory is interpolated to generate an estimated position, $\mathbf{r}_{estimate}$, corresponding to $t_{estimate}$.

(c) A new estimated uncorrected time event, $t_{estimate_{new}}$, is computed using $\mathbf{r}_{estimate}$.

(d) If the error between $t_{estimate_{new}}$ and $t_{estimate}$ is less than 1 ps (1×10^{-12} s) then a new barycentric time event, $t_{SSB_{new}}$, is computed by correcting $t_{estimate_{new}}$. Otherwise, the process is repeated by setting $t_{estimate} = t_{estimate_{new}}$.

(e) If the error between the barycentric time event, t_{SSB}, sent to the iteration routine and $t_{SSB_{new}}$ is less than 10 ps, then $t_{estimate_{new}}$ is returned and stored as the t_{SC} value corresponding to the t_{SSB} value. Otherwise, the process is repeated by setting $t_{estimate} = t_{estimate_{new}}$. Note that the tolerance in this step is greater than 1 ps to both speed up processing time and avoid infinite loops.

5. The spacecraft trajectory is interpolated to obtain position coordinates corresponding to all t_{SC} values.

6. The t_{SC} values are corrected to the SSB using the interpolated positions, thus generating a different set of SSB arrival times, $t_{SSB_{SC}}$.

7. The difference between t_{SSB} and the new $t_{SSB_{SC}}$ is computed to verify that errors are less than 10 ps.

After performing this routine, XPRESS returns the t_{SSB}, t_{SC}, and $t_{SSB_{SC}}$ values for plotting and writes the t_{SC} values to a text file in the same format as the XPRESS data headers. A detailed description of the time transfer equations used in the uncorrection and correction process follows.

3.2 XPRESS Delay Terms and Simulation Modes

Pulsar timing requires the transformation of photon time events received at a detector to the center of mass of the Solar System (SSB), which is a very good approximation of an inertial reference frame [23, 24]. This transformation is generally grouped into four categories as shown in the following equation:

$$t_{SSB} = t_{SC} - (\Delta t_{DM} + \Delta t_{R\odot} + \Delta t_{S\odot} + \Delta t_{E\odot}) \tag{3.3}$$

where the symbol $\odot$ relates to the solar system. The term Δt_{DM} is a delay term due to the interstellar transmission medium. This term is a function of the signal frequency and is significant for radio and optical observations, but it is considered negligible in X-ray pulsar timing equations [34]. The term $\Delta t_{R\odot}$ is a large geometric delay term that incorporates the classical geometry of the Solar System and the effect of wavefront curvature [23], and is called *Römer delay*. The term $\Delta t_{S\odot}$ is the *Shapiro delay*, which is delay due to the curvature of spacetime caused by masses present in the Solar System such as planets and other large massive bodies [23, 24, 34]. The final term, $\Delta t_{E\odot}$, is the *Einstein delay*, which is delay due to gravitational redshift and time dilation [24]. The Shapiro and Einstein delays result from general relativistic corrections, while the main component of Römer delay is due to geometry of the spacecraft with respect to the SSB. It should be noted that the Einstein delay represented in Equation 3.3 is not apparent in this discussion, thus the interested reader is referred to [34] and the references contained within.

The six different simulation modes available in XPRESS are implementations of the work presented in [34], which identifies the direct time transfer equations between any spacecraft and the SSB. These simulation modes are combinations of different components of the geometric and relativistic delay terms defined in Table 3.1 below. Included in these components are additional terms due to *proper motion* of the source pulsar,

which is the motion of the pulsar with respect to the SSB and is generally described by both radial and transverse motion. Proper motion also adds additional geometric and relativistic corrections into the individual Römer components.

Table 3.1: Components of geometric and relativistic delay terms

Component Name	**Component Definition**
Geometric $(\Delta t_{R\odot})$	$\frac{\hat{\mathbf{n}}_0 \cdot \mathbf{r}}{c}$
Römer 1 $(\Delta t_{R\odot}, \Delta t_{E\odot})$	$\frac{1}{c}\left[-\frac{r^2}{2D_0} + \frac{(\hat{\mathbf{n}}_0 \cdot \mathbf{r})^2}{2D_0}\right]$
Römer 2 $(\Delta t_{R\odot}, \Delta t_{E\odot})$	$\frac{1}{c}\left[\frac{(\hat{\mathbf{n}}_0 \cdot \mathbf{b})(\hat{\mathbf{n}}_0 \cdot \mathbf{r})}{D_0} - \frac{\mathbf{b} \cdot \mathbf{r}}{D_0}\right]$
Römer 3 $(\Delta t_{R\odot}, \Delta t_{E\odot})$	$\frac{1}{c}\left\{\frac{\hat{\mathbf{n}}_0 \cdot \mathbf{r}}{D_0^2}\left[(\mathbf{b} \cdot \mathbf{V}\Delta t_N) - (\mathbf{b} \cdot \mathbf{r}) - \frac{b^2}{2}\right]\right\}$ $+\frac{1}{c}\left\{\frac{\hat{\mathbf{n}}_0 \cdot \mathbf{b}}{D_0^2}\left[(\mathbf{r} \cdot \mathbf{V}\Delta t_N) - (\mathbf{b} \cdot \mathbf{r}) - \frac{r^2}{2}\right]\right\}$ $+\frac{1}{c}\left[\frac{(\hat{\mathbf{n}}_0 \cdot \mathbf{V}\Delta t_N)(\mathbf{b} \cdot \mathbf{r})}{D_0^2}\right]$
Shapiro 1 $(\Delta t_{S\odot})$	$\frac{2\mu_s}{c^3} \ln\left\lvert\frac{\hat{\mathbf{n}}_0 \cdot \mathbf{p} + p}{\hat{\mathbf{n}}_0 \cdot \mathbf{b} + b}\right\rvert$

Continued on next page

Table 3.1 – continued from previous page

Component Name	Component Definition
Shapiro 2 $(\Delta t_{S\odot})$	$\sum_{k=1}^{B_{SS}} \frac{2\mu_k}{c^3} \ln \left\lvert \frac{\hat{\mathbf{n}}_N \cdot \mathbf{p}_k + p_k}{\hat{\mathbf{n}}_N \cdot \mathbf{b}_k + b_k} \right\rvert$
Proper Motion 1 $(\Delta t_{R\odot}, \Delta t_{E\odot})$	$\frac{1}{c}\left[\frac{\mathbf{r}\cdot\mathbf{V}\Delta t_N}{D_0} - \frac{(\hat{\mathbf{n}}_0\cdot\mathbf{V}\Delta t_N)(\hat{\mathbf{n}}_0\cdot\mathbf{r})}{D_0}\right]$
Proper Motion 2 $(\Delta t_{R\odot}, \Delta t_{E\odot})$	$\frac{1}{c}\left\{\frac{\hat{\mathbf{n}}_0\cdot\mathbf{r}}{D_0^2}\left[(\mathbf{r}\cdot\mathbf{V}\Delta t_N) - \frac{r^2}{2}\right] + \frac{\hat{\mathbf{n}}_0\cdot\mathbf{V}\Delta t_N}{D_0^2}\left[\frac{r^2}{2} - (\mathbf{r}\cdot\mathbf{V}\Delta t_N)\right]\right\}$

The component definitions presented in Table 3.1 are taken directly from the time transfer equation in Section 3.2.4 below (Equation 3.8). This equation is a simplification of the direct time transfer equation presented in [34] and shown as Equation 3.9 in Section 3.2.5 below. NASA's Swift spacecraft, a gamma-ray observatory operating in LEO [36], is a good analog of a Mothership spacecraft operating with a large detector and a known position, thus a simulation using the orbital dynamics of a day-long trajectory of Swift was performed using all six modes. A sample time time delay for each mode is presented and the differences between the delays from each previous mode are examined in the following sections. Figure 3.2 below shows the geometry of the vectors used in the component equations in Table 3.1. These variables will be described as they emerge in the subsequent sections that describe the equations used in the six different XPRESS simulation modes.

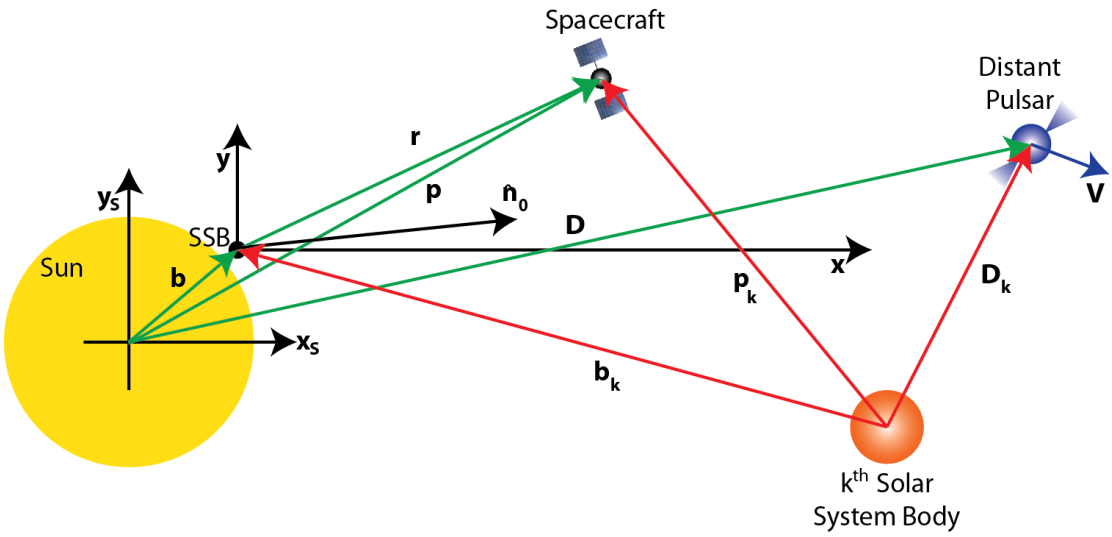

Figure 3.2: Geometry of vectors used in pulsar timing equations.

3.2.1 XPRESS Simulation Mode None

The first XPRESS simulation mode includes the Geometric delay term defined in Table 3.1 only. This mode is referred to as Mode None due to the fact that no relativistic effects are included in the following time transfer equation:

$$(t_{SSB} - t_{SC}) = \frac{\hat{\mathbf{n}}_0 \cdot \mathbf{r}}{c}. \tag{3.4}$$

Here, the unit direction to the source pulsar is represented by $\hat{\mathbf{n}}_0$, and the spacecraft position is represented by $\mathbf{r}$.

This single delay term is the largest of those presented in Table 3.1. For example, a simulated geometric delay of 251.9798030 s, or 75,525,769.78 km when scaled by c, was generated for the first simulated time event along the spacecraft's trajectory, which represents the order of magnitude of the delay within the vehicle's orbit. The remaining modes use this same time event as a benchmark to refine the delay by including relativistic effects.

3.2.2 XPRESS Simulation Modes A with and A without Proper Motion

The XPRESS simulation Mode A is implemented as two separate modes. Mode A without Proper Motion includes the Geometric, Römer 1 and 2, and Shapiro 1 delay terms defined in Table 3.1 as follows:

$$(t_{SSB} - t_{SC}) = \frac{1}{c}\left[\begin{array}{l}\hat{\mathbf{n}}_0 \cdot \mathbf{r} - \dfrac{r^2}{2D_0} + \dfrac{(\hat{\mathbf{n}}_0 \cdot \mathbf{r})^2}{2D_0} \\ + \dfrac{(\hat{\mathbf{n}}_0 \cdot \mathbf{b})(\hat{\mathbf{n}}_0 \cdot \mathbf{r})}{D_0} - \dfrac{\mathbf{b} \cdot \mathbf{r}}{D_0}\end{array}\right] + \frac{2\mu_s}{c^3} \ln \left| \frac{\hat{\mathbf{n}}_0 \cdot \mathbf{p} + p}{\hat{\mathbf{n}}_0 \cdot \mathbf{b} + b} \right|, \tag{3.5}$$

while simulation Mode A with Proper Motion adds the Proper Motion 1 delay term defined in Table 3.1 to Equation 3.5 as follows:

$$(t_{SSB} - t_{SC}) = \frac{1}{c}\left[\begin{array}{l}\hat{\mathbf{n}}_0 \cdot \mathbf{r} - \dfrac{r^2}{2D_0} + \dfrac{(\hat{\mathbf{n}}_0 \cdot \mathbf{r})^2}{2D_0} \\ + \dfrac{(\hat{\mathbf{n}}_0 \cdot \mathbf{b})(\hat{\mathbf{n}}_0 \cdot \mathbf{r})}{D_0} - \dfrac{\mathbf{b} \cdot \mathbf{r}}{D_0} \\ + \dfrac{\mathbf{r} \cdot \mathbf{V}\Delta t_N}{D_0} - \dfrac{(\hat{\mathbf{n}}_0 \cdot \mathbf{V}\Delta t_N)(\hat{\mathbf{n}}_0 \cdot \mathbf{r})}{D_0}\end{array}\right] + \frac{2\mu_s}{c^3} \ln \left| \frac{\hat{\mathbf{n}}_0 \cdot \mathbf{p} + p}{\hat{\mathbf{n}}_0 \cdot \mathbf{b} + b} \right|. \tag{3.6}$$

The additional variables included in Equations 3.5 and 3.6 are the magnitude of the position vector, r, the magnitude of the distance from the SSB to the pulsar, D_0, the proper motion vector, $\mathbf{V}$, the change in time from the epoch of the pulsar timing model and ephemeris data to the photon time event in seconds, Δt_N, the position of the SSB with respect to the sun, $\mathbf{b}$, the magnitude of the vector $\mathbf{b}$, b, and the *gravitational parameter* of the Sun, μ_s. The product, $\mathbf{V}\Delta t_N$, incorporates the proper motion of the pulsar from the epoch of the pulsar timing model and ephemeris data to the current detected photon time event, thus accounting for the change in the unit vector to the source pulsar from the time at which the pulsar observation used in the XPRESS source data header was recorded. The Shapiro 1 delay term incorporates the delay due to the curvature of spacetime caused by the Sun only, while the Römer 1 and 2 delay terms incorporate additional geometric delay terms scaled by D_0.

Mode A without Proper Motion yielded a simulated delay of 251.9798539 s, or 75,525,785.04 km when scaled by c, resulting in a difference of 50.89186243 μs, or 15.25379034 km when scaled by c, from Mode None. Mode A with Proper Motion yielded a simulated delay of 251.9798539 s as well. However, the resulting difference was 5.673172154 ns, or 1.700416815 m when scaled by c, from Mode A with Proper Motion. These results indicate that utilization of Mode A with Proper Motion refines the error in the time transfer equations to the meter level.

3.2.3 XPRESS Simulation Mode B

The XPRESS simulation Mode B refines the previous modes by including the Shapiro 2 delay term defined in Table 3.1. This term sums the individual Shapiro delays due to the curvature of spacetime caused by the Sun, Mercury, Venus, Earth, the Moon, Mars, Jupiter, Saturn, Uranus, Neptune, and Pluto. Therefore, the Shapiro 1 delay term is excluded from Mode B due to the fact that the Shapiro 2 delay term encompasses the delay included in Shapiro 1 (curvature of spacetime caused by the Sun). The resulting Mode B time transfer equation is as follows:

$$(t_{SSB} - t_{SC}) = \frac{1}{c}\left[\begin{array}{l} \hat{\mathbf{n}}_0 \cdot \mathbf{r} - \dfrac{r^2}{2D_0} + \dfrac{(\hat{\mathbf{n}}_0 \cdot \mathbf{r})^2}{2D_0} \\ + \dfrac{(\hat{\mathbf{n}}_0 \cdot \mathbf{b})(\hat{\mathbf{n}}_0 \cdot \mathbf{r})}{D_0} - \dfrac{\mathbf{b} \cdot \mathbf{r}}{D_0} \\ + \dfrac{\mathbf{r} \cdot \mathbf{V}\Delta t_N}{D_0} - \dfrac{(\hat{\mathbf{n}}_0 \cdot \mathbf{V}\Delta t_N)(\hat{\mathbf{n}}_0 \cdot \mathbf{r})}{D_0} \end{array}\right] + \sum_{k=1}^{B_{SS}} \frac{2\mu_k}{c^3} \ln \left| \frac{\hat{\mathbf{n}}_N \cdot \mathbf{p}_k + p_k}{\hat{\mathbf{n}}_N \cdot \mathbf{b}_k + b_k} \right|, \tag{3.7}$$

where the sum over the k Solar System bodies, B_{SS}, mentioned above (i.e. $k = 1$ for the Sun, $k = 2$ for Venus, and so on) is represented by $\sum_{k=1}^{B_{SS}}$, the gravitational parameter of the kth Solar System body is represented by μ_k, the current unit direction to the source pulsar (taking proper motion into account) is given by $\hat{\mathbf{n}}_N$, the position and distance of the spacecraft with respect to the kth Solar System body are given by $\mathbf{p}_k$ and p_k, respectively, and the position and distance of the SSB with respect to the kth

Solar System body are given by $\mathbf{b}_k$ and b_k, respectively. This geometry is illustrated in Figure 3.2 above.

Mode B yielded a simulated delay of 251.9798539 s, which is the same delay seen in both Mode A implementations. However, the difference between Mode B and Mode A with Proper Motion was found to be 2.498040885 ns, or 0.7487364406 m. This means that Mode B refines the error in the time transfer equation to sub-meter level accuracy. Therefore, for most applications Mode B is sufficient for testing XNAV algorithms. However, to provide a complete simulation of the geometric and relativistic effects on pulsar timing, further refinements must be made.

3.2.4 XPRESS Simulation Mode C

The XPRESS simulation Mode C incorporates all delay components defined in Table 3.1. The difference between Mode B and Mode C is that Mode C includes both the Römer 3 and Proper Motion 2 components defined in Table 3.1 as seen in the following:

$$(t_{SSB}-t_{SC}) = \frac{1}{c}\left[\begin{array}{l} \hat{\mathbf{n}}_0\cdot\mathbf{r} - \dfrac{r^2}{2D_0} + \dfrac{(\hat{\mathbf{n}}_0\cdot\mathbf{r})^2}{2D_0} + \dfrac{(\hat{\mathbf{n}}_0\cdot\mathbf{b})(\hat{\mathbf{n}}_0\cdot\mathbf{r})}{D_0} \\ -\dfrac{\mathbf{b}\cdot\mathbf{r}}{D_0} + \dfrac{\mathbf{r}\cdot\mathbf{V}\Delta t_N}{D_0} - \dfrac{(\hat{\mathbf{n}}_0\cdot\mathbf{V}\Delta t_N)(\hat{\mathbf{n}}_0\cdot\mathbf{r})}{D_0} \\ +\dfrac{\hat{\mathbf{n}}_0\cdot\mathbf{r}}{D_0^2}\left[(\mathbf{r}\cdot\mathbf{V}\Delta t_N) - \dfrac{r^2}{2}\right] \\ +\dfrac{\hat{\mathbf{n}}_0\cdot\mathbf{V}\Delta t_N}{D_0^2}\left[\dfrac{r^2}{2} - (\mathbf{r}\cdot\mathbf{V}\Delta t_N)\right] \\ +\dfrac{(\hat{\mathbf{n}}_0\cdot\mathbf{V}\Delta t_N)(\mathbf{b}\cdot\mathbf{r})}{D_0^2} \\ +\dfrac{\hat{\mathbf{n}}_0\cdot\mathbf{r}}{D_0^2}\left[(\mathbf{b}\cdot\mathbf{V}\Delta t_N) - (\mathbf{b}\cdot\mathbf{r}) - \dfrac{b^2}{2}\right] \\ +\dfrac{\hat{\mathbf{n}}_0\cdot\mathbf{b}}{D_0^2}\left[(\mathbf{r}\cdot\mathbf{V}\Delta t_N) - (\mathbf{b}\cdot\mathbf{r}) - \dfrac{r^2}{2}\right] \end{array}\right] + \sum_{k=1}^{B_{SS}} \frac{2\mu_k}{c^3}\ln\left|\frac{\hat{\mathbf{n}}_N\cdot\mathbf{p}_k + p_k}{\hat{\mathbf{n}}_N\cdot\mathbf{b}_k + b_k}\right|. \tag{3.8}$$

There are no variables that appear in Equation 3.8 that were not seen in Equation 3.7, and the major difference is that Mode C now includes terms that are scaled by

${D_0}^2$. Because D_0 is on the order of kiloparsecs (kpc) distant (about $3.1 \times 10^{16} \frac{km}{kpc}$), the difference between Modes B and C is expected to be very small.

Mode C yielded a simulated delay of 251.9798539 s, which is the same delay seen in the previous three implementations. However, the difference between Mode C and Mode B was found to be .005684341886 ps, or 17.037647123 μm. Thus, the expectation that the difference between Modes B and C would be very small is confirmed. This implies that processing time for testing XNAV algorithms can be increased by implementing Mode B. However, the difference in processing time while implementing Mode C instead of Mode B is small compared to implementing Mode D as described in the following section.

3.2.5 XPRESS Simulation Mode D

The XPRESS simulation Mode D implements the direct time transfer equation derived in [34]. As shown in Figures 2.1 and 2.3, the pulses from a distant pulsar arrive in the Solar System as planar wavefronts due to the vast astronomical distances to the source pulsar. This allows the assumption that the unit directions to the source pulsar from the barycenter and the spacecraft are parallel, and thus the same. All previous simulation modes described above make this assumption, while Mode D does not. Therefore, the

resulting time transfer equation is as follows:

$$
\begin{aligned}
(t_{SSB} - t_{SC}) = \frac{1}{c}\left[(\hat{\mathbf{n}}_{SC}\cdot\mathbf{p}) - (\hat{\mathbf{n}}_{SSB}\cdot\mathbf{p})\right] + \frac{1}{c}(\hat{\mathbf{n}}_{SSB} - \hat{\mathbf{n}}_{SC})\cdot\mathbf{D} \\
+ \sum_{k=1}^{B_{SS}} \frac{2\mu_k}{c^3}\ln\left|\left(\frac{\hat{\mathbf{n}}_{SC}\cdot\mathbf{p}_k + p_k}{\hat{\mathbf{n}}_{SSB}\cdot\mathbf{b}_k + b_k}\right)\left(\frac{\hat{\mathbf{n}}_{SSB}\cdot\mathbf{D}_k + D_k}{\hat{\mathbf{n}}_{SC}\cdot\mathbf{D}_k + D_k}\right)\right| \\
+ \frac{2\mu_s}{c^5 D_{y_{SSB}}^2}\Bigg\{\hat{\mathbf{n}}_{SSB}\cdot(\mathbf{D}-\mathbf{b})\left[1 + \left(\frac{\hat{\mathbf{n}}_{SSB}\cdot\mathbf{D}}{D}\right)^2 - 2\frac{D_{y_{SSB}}^2}{bD}\right] \\
+ 2(\hat{\mathbf{n}}_{SSB}\cdot\mathbf{D})\left(\frac{b}{D} - 1\right) \\
+ \frac{15}{8}D_{y_{SSB}}\left[\arctan\left(\frac{\hat{\mathbf{n}}_{SSB}\cdot\mathbf{D}}{D_{y_{SSB}}}\right) - \arctan\left(\frac{\hat{\mathbf{n}}_{SSB}\cdot\mathbf{b}}{D_{y_{SSB}}}\right)\right]\Bigg\} \\
- \frac{2\mu_s}{c^5 D_{y_S}^2}\Bigg\{\hat{\mathbf{n}}_{SC}\cdot(\mathbf{D}-\mathbf{p})\left[1 + \left(\frac{\hat{\mathbf{n}}_{SC}\cdot\mathbf{D}}{D}\right)^2 - 2\frac{D_{y_S}^2}{pD}\right] \\
+ 2(\hat{\mathbf{n}}_{SC}\cdot\mathbf{D})\left(\frac{p}{D} - 1\right) \\
+ \frac{15}{8}D_{y_S}\left[\arctan\left(\frac{\hat{\mathbf{n}}_{SC}\cdot\mathbf{D}}{D_{y_S}}\right) - \arctan\left(\frac{\hat{\mathbf{n}}_{SC}\cdot\mathbf{p}}{D_{y_S}}\right)\right]\Bigg\}.
\end{aligned}
\tag{3.9}
$$

Here, the variables $\hat{\mathbf{n}}_{SC}$ and $\hat{\mathbf{n}}_{SSB}$ are the unit direction to the source pulsar from the spacecraft and SSB, respectively, the vector $\mathbf{D}$ is the position of the source pulsar with respect to the SSB, the vector $\mathbf{D_k}$ is the is the position of the source pulsar with respect to the kth Solar System body, and the variables $D_{y_{SSB}}$ and D_{y_S} are the distances to the source pulsar from the SSB and Sun projected onto the y-axes of the SSB and Sun, respectively.

Because pulsar distances are on the order of $3.1 \times 10^{16} km$ (kiloparsecs), double precision logic is not sufficient when making computations involving $\mathbf{D_k}$ and its associated magnitudes. Thus, symbolic math must be utilized in Matlab to make computations precise enough for nanosecond-level accuracy. While implementing this approach, it was discovered that simulation times on the order of hours were required to perform Mode

D simulations. This inhibits the use of Mode D in algorithm verification and testing. However, the difference between implementing Mode C and Mode D in the simulation was found to be 24.67004379 ps, or 7.394338853 mm, thus ensuring that Mode C provides sufficient precision in the implementation of high-order time transfer equations for testing and verifying XNAV algorithms.

The implementation of Mode C has proven to be a sufficient simulation model to test and verify XNAV algorithms, so it follows that XPRESS delivers the required precision to fill the need for a simulation system designed to assist analysis and algorithm verification of X-ray based systems. A more in-depth discussion on the delay components defined in Table 3.1 follows in order to investigate the specific effects each term has on the time transfer equations.

3.3 Simulation Results of XPRESS Delay Term Components

Implementation of the six XPRESS simulation modes were discussed above. The following discussion explores the effects that the individual components of the geometric and relativistic delay terms defined in Table 3.1 have on spacecraft orbiting different Solar System bodies. Two sets of simulations were performed for three currently operating spacecraft: NASA's Swift, NASA's Mercury Messenger, and the ESA's Mars Express. One set simulated the pulsar B1937+21, while the other set simulated pulsar B1821-24. For each spacecraft, a 24 hour long trajectory beginning at midnight on September 1, 2012 was produced using JPL's HORIZONS online ephemeris system [37]. This date was chosen because the inaugural flight of the test bed described in Chapter 4 occurred on September 1, 2012. The hope is that future flights of the test bed can examine observations made concurrently by the gamma ray observatory, Swift. It is also hoped that

simulating detectors onboard spacecraft orbiting other planetary bodies such as Mercury and Mars will increase the viability of an XNAV-based interplanetary constellation of spacecraft. These simulations were carried out using XPRESS Mode C, or Equation 3.8, as that mode includes all delay components as defined in Table 3.1 above. In order to easily compare the results from each figure presented in the following sections, the time history of each spacecraft's trajectory is plotted as the index of the spacecraft's position in time. Thus, each index corresponds to the same simulated time event.

3.3.1 Geometric Delay Component Simulation Results

Figure 3.3 below shows the simulation results for the Geometric delay component defined in Table 3.1 for each simulation scenario.

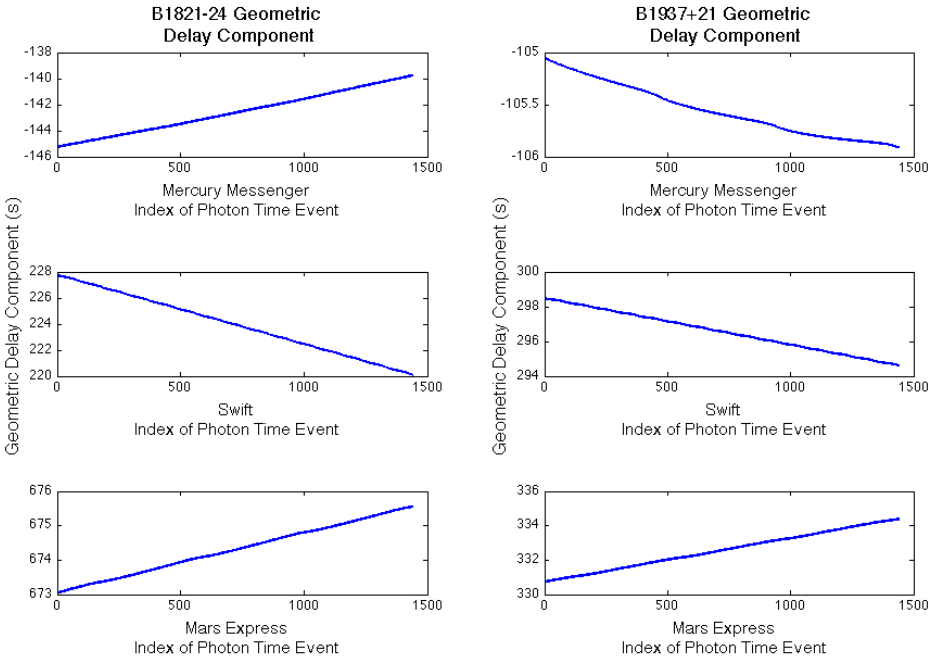

Figure 3.3: Simulation results for the Geometric delay component defined in Table 3.1.

As seen in Figure 3.3, the Geometric delay component is large for each scenario. This is the largest delay encountered in the time transfer equations, and is due to the geometry seen in Figure 3.2. However, the magnitude of the delays are not intuitive. For instance, the time is takes light to reach Earth from the SSB is on the order of about 8 minutes (480 s), while the results in Figure 3.2 indicate delays of about 220 s and 300 s. The reason behind the smaller delay seen in the results is due to the scalar product, $\hat{\mathbf{n}}_0 \cdot \mathbf{r}$. This corresponds to the projection of the spacecraft position, $\mathbf{r}$, onto the unit direction to the source pulsar, $\hat{\mathbf{n}}_0$, which results in a light time less than the intuitive expectation of 8 minutes. Figure 3.4 below illustrates this more clearly.

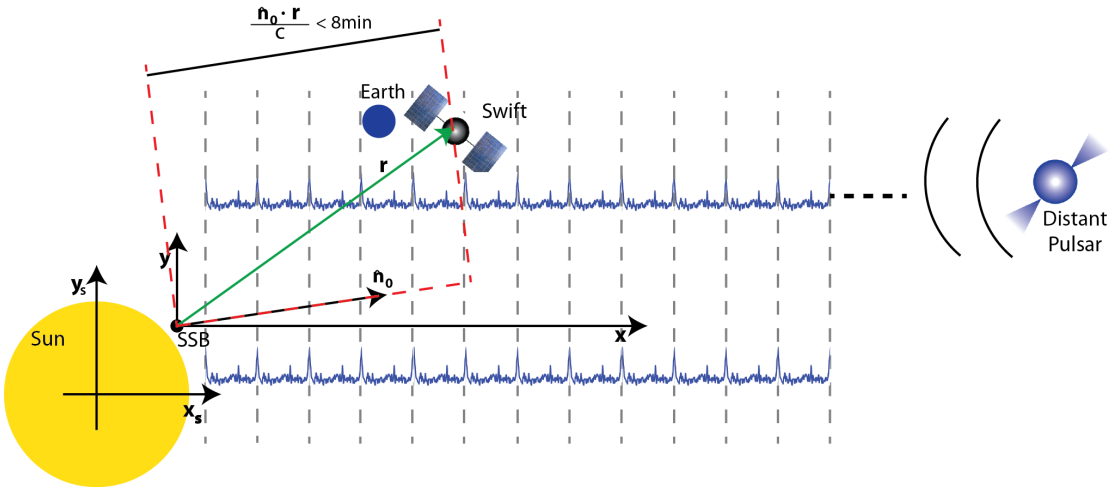

Figure 3.4: Illustration showing that the Geometric delay component projects the spacecraft position, $\mathbf{r}$ onto the unit vector to the source pulsar, $\hat{\mathbf{n}}_0\cdot$, resulting in a time transfer less than the light time between Earth and the SSB. Note: Illustration is not to scale.

3.3.2 Römer 1 Delay Component Simulation Results

Figure 3.5 below shows the simulation results for the Römer 1 delay component defined in Table 3.1 for each simulation scenario. The results indicate that the Römer 1 delay component has a magnitude larger than 1 ns. This implies that the Römer 1 component

should be included in any simulation striving for position accuracies at the meter level.

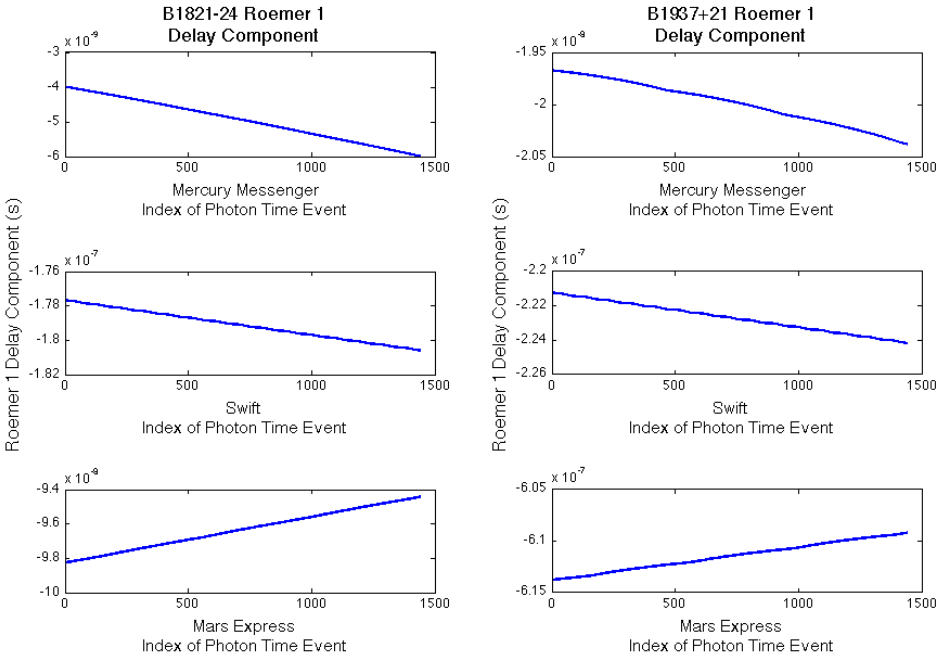

Figure 3.5: Simulation results for the Roemer 1 delay component defined in Table 3.1.

3.3.3 Römer 2 Delay Component Simulation Results

Figure 3.6 below shows the simulation results for the Römer 2 delay component defined in Table 3.1 for each simulation scenario. The results indicate that the Römer 2 delay component is generally smaller than 1 ns. However, the magnitude can be on the order of 1 ns as seen in the Mars Express simulation results for pulsar B1937+21 in Figure 3.6. This implies that the Römer 2 component should be simulated when position accuracies at the meter level are required.

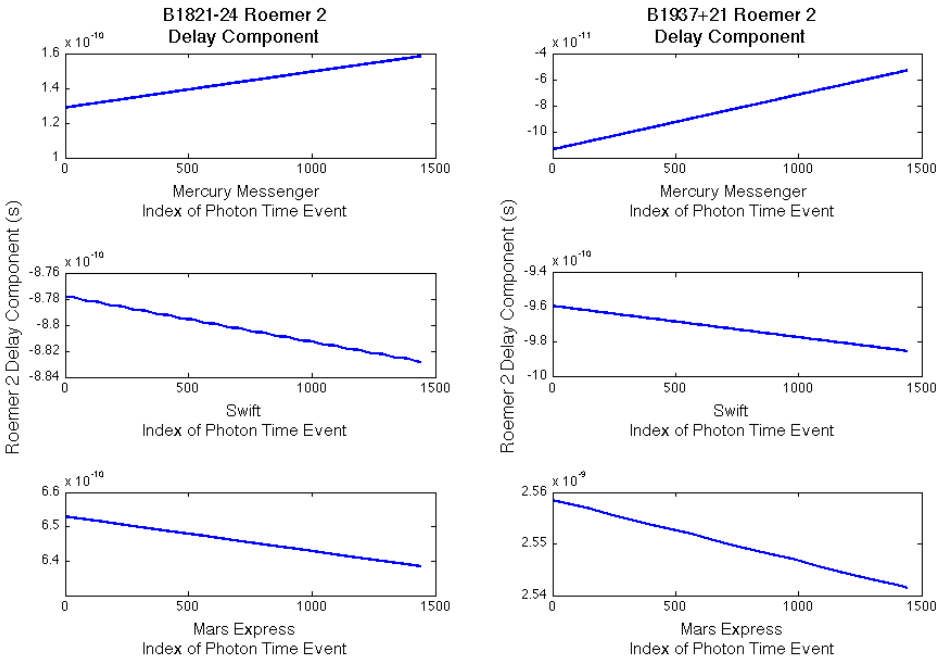

Figure 3.6: Simulation results for the Roemer 2 delay component defined in Table 3.1.

3.3.4 Römer 3 Delay Component Simulation Results

Figure 3.7 below shows the simulation results for the Römer 3 delay component defined in Table 3.1 for each simulation scenario. The results show that the largest Römer 3 delay component is on the order of 1×10^{-19} s, which is negligible when requiring accuracies on the order of 1 ns. This implies that the Römer 3 component can be ignored in any simulation requiring position accuracies at the meter level.

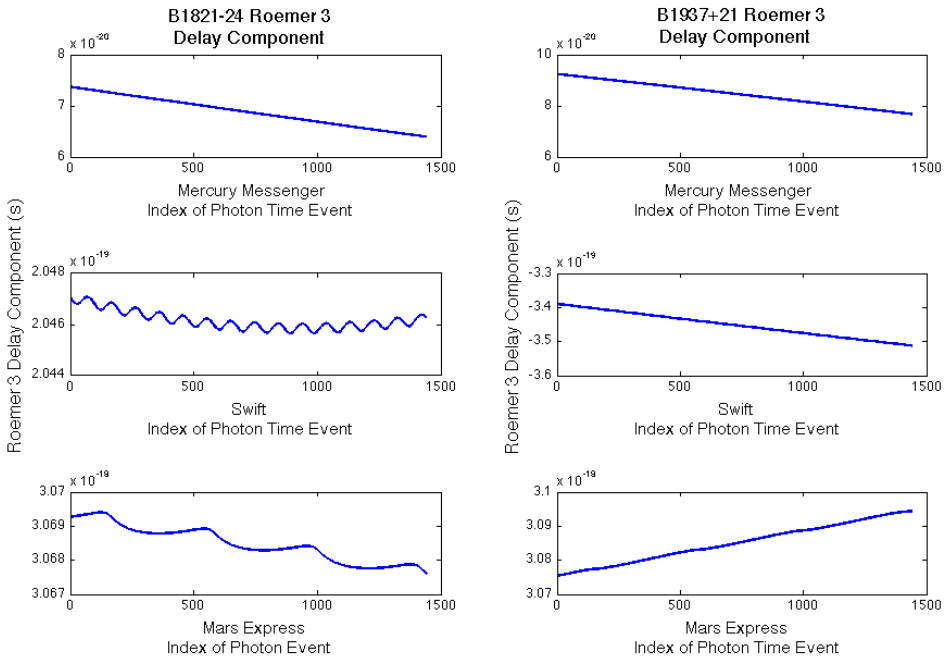

Figure 3.7: Simulation results for the Roemer 3 delay component defined in Table 3.1.

3.3.5 Shapiro 1 Delay Component Simulation Results

Figure 3.8 below shows the simulation results for the Shapiro 1 delay component defined in Table 3.1 for each simulation scenario. The results show that the Shapiro 1 delay

component, or Shapiro delay due to the Sun alone, is one of the largest delay terms in the time transfer equations. The resulting delay for all simulation scenarios is on the order of tens of μs. This implies that the Shapiro 1 delay component refines the position accuracy of the time transfer equations at the kilometer level. Thus, the Shapiro 1 delay component must be included in any simulation requiring precise timing and positioning.

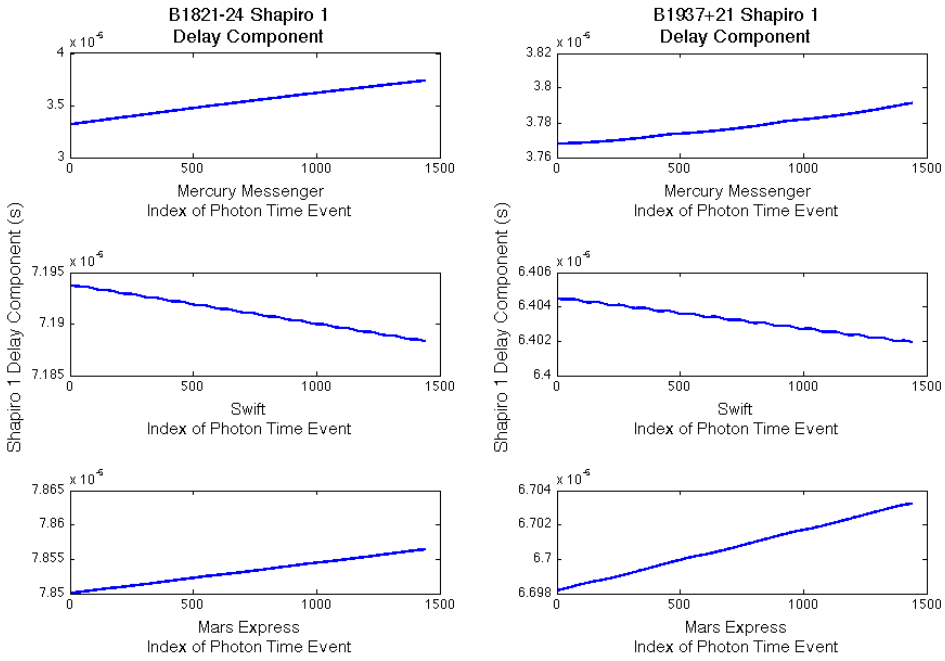

Figure 3.8: Simulation results for the Shapiro 1 delay component defined in Table 3.1.

3.3.6 Shapiro 2 Delay Component Simulation Results

Figure 3.9 below shows the simulation results for the Shapiro 2 delay component defined in Table 3.1 for each simulation scenario. The Shapiro 2 delay component includes Shapiro delay due to the Sun, Mercury, Venus, Earth, the Moon, Mars, Jupiter, Saturn, Uranus, Neptune, and Pluto.

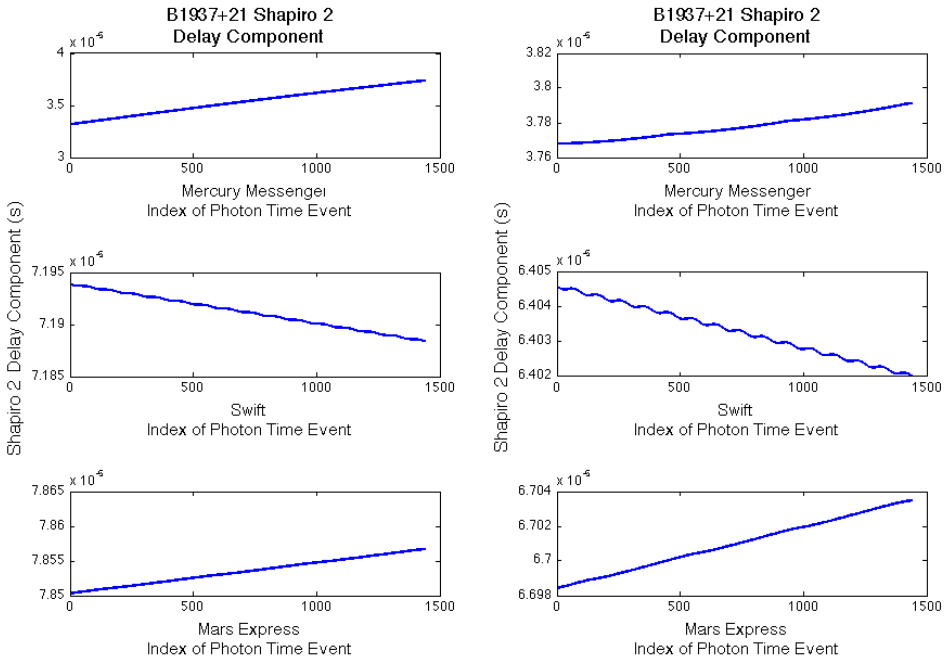

Figure 3.9: Simulation results for the Shapiro 2 delay component defined in Table 3.1.

The resulting delays shown in Figure 3.9 appear to be the same delays as the results from the Shapiro 1 delay component simulation in Figure 3.8. Therefore, the difference between the Shapiro 2 and Shapiro 1 delay components was taken, and the resulting differences are shown in Figure 3.10.

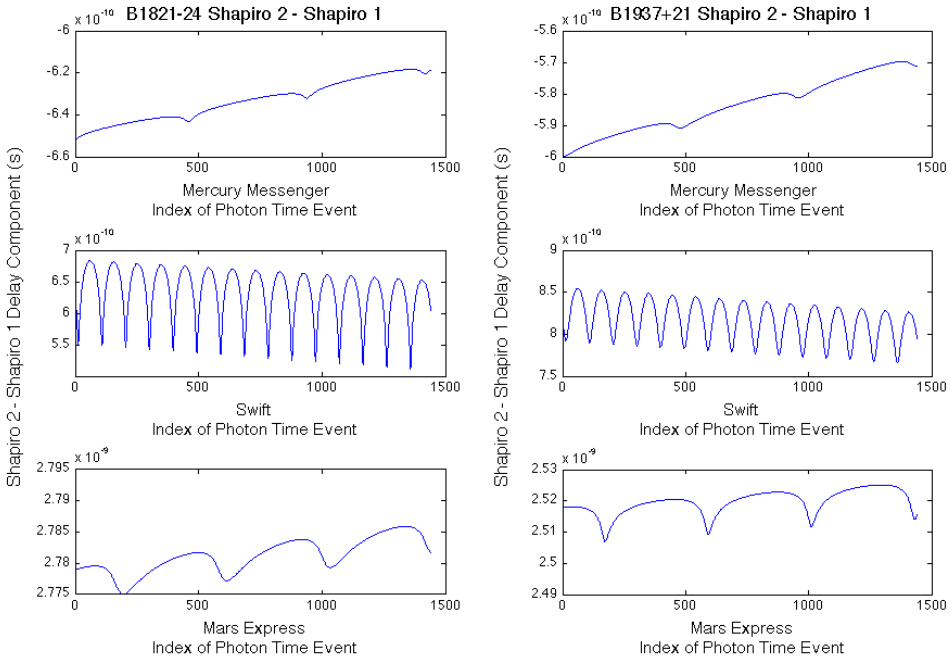

Figure 3.10: Difference between the simulation results from the Shapiro 1 and 2 Delay components defined in Table 3.1

As seen in the Mars Express simulation results in Figure 3.10, the difference between the Shapiro 2 and Shapiro 1 delay components can be greater than 1 ns, thus indicating that it is important to include the Shapiro delay due to Solar System bodies other than the Sun when requiring position accuracies at the meter level. It should also be noted that Mars is closer to Jupiter than Earth or Mercury. This implies that Jupiter's effect on the curvature of spacetime will be greater for objects closer to Jupiter, which is the most massive object in the Solar System other than the Sun. Figure 3.10 supports this argument as the Shapiro 2 delay component has the largest effect on the Mars Express spacecraft. Therefore, the most important considerations when applying Shapiro delay in the time transfer equation are to include massive bodies near the spacecraft, as well

as the largest massive bodies in the Solar System (i.e. Jupiter and the Sun).

3.3.7 Proper Motion 1 Delay Component Simulation Results

Figure 3.11 below shows the simulation results for the Proper Motion 1 delay component defined in Table 3.1 for each simulation scenario. The results shown in Figure 3.11 are somewhat misleading as the scenarios that include pulsar B1821-24 show a delay of zero. This is due to the fact that at the time of simulation, there was no data on the proper motion of pulsar B1821-24 available, thus the proper motion vector, $\mathbf{V} = \{\mathbf{0}\}$. However, the results from the scenarios including pulsar B1937+21 indicate that the magnitude of the Proper Motion 1 delay component is greater than 1 ns, thus implying that the Proper Motion 1 delay component should be included in simulations requiring precise timing and positioning.

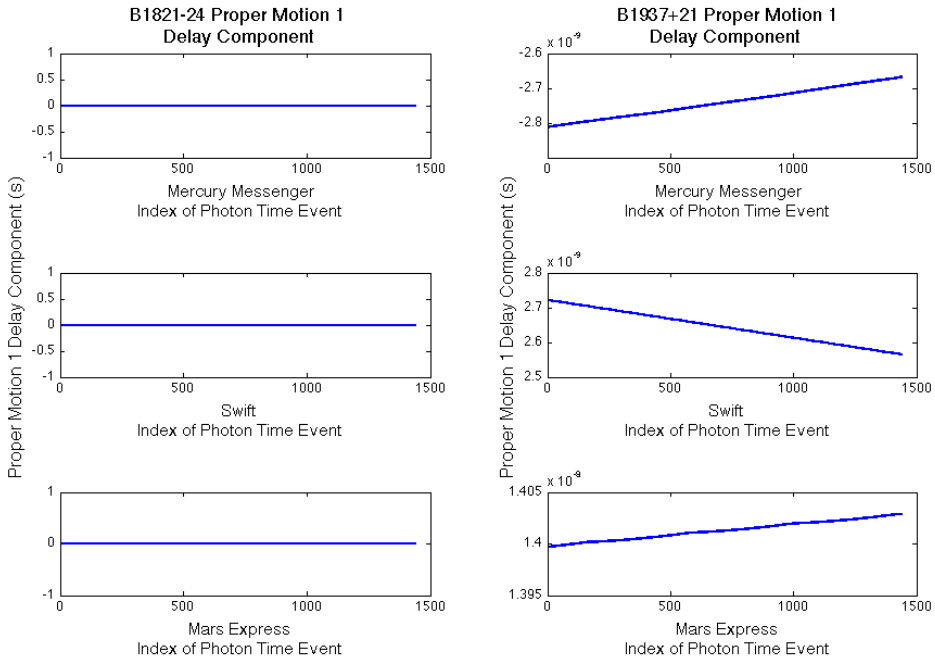

Figure 3.11: Simulation results for the Proper Motion 1 delay component defined in Table 3.1.

3.3.8 Proper Motion 2 Delay Component Simulation Results

Figure 3.12 below shows the simulation results for the Proper Motion 2 delay component defined in Table 3.1 for each simulation scenario. The results shown in Figure 3.12 for the scenarios including pulsar B1821-24 are counterintuitive to the fact that the proper motion vector $\mathbf{V} = \{\mathbf{0}\}$. However, there are other terms included in the Proper Motion 2 component equation defined in Table 3.1 that make the delay non-zero for the B1821-24 scenarios. The Proper Motion 2 delay component simulation yielded negligible delays for all scenarios of less than 10×10^{-16} s. This implies that the Proper Motion 2 delay component can be ignored when requiring simulation accuracies at the nanosecond level.

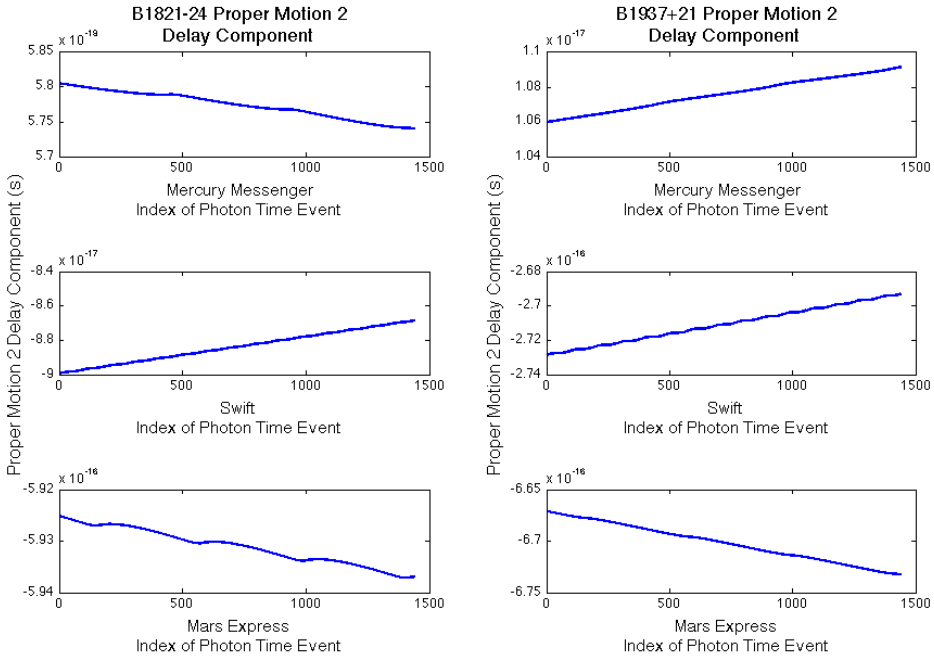

Figure 3.12: Simulation results for the Proper Motion 2 delay component defined in Table 3.1.

3.3.9 XPRESS Delay Component Conclusions

Based on the results from the simulations presented above, an XPRESS mode that includes the Geometric, Römer 1, Römer 2, Shapiro 2, and Proper Motion 1 components defined in Table 3.1 will provide the required sub-meter level accuracies. This implies that XPRESS Mode B is the optimal simulation mode when considering processing time and sub-meter levels of accuracy.

Chapter 4

High Altitude X-Ray Detector Test Bed

Algorithmic and hardware challenges that need to be solved to realize XNAV were discussed above. In order to verify such algorithms and signal models, a platform capable of testing detector hardware must be built and flown. Therefore, the University of Minnesota has developed the High Altitude X-ray Detector Testbed (HAXDT), which is a small payload designed to fly on a high altitude scientific balloon to test and validate the performance of a compact X-ray detector and its associated flight hardware. This payload is configured to be flown on the High Altitude Student Platform (HASP), which is designed to carry twelve student payloads to altitudes around 36 kilometers with flight durations up to 20 hours using a small volume, zero pressure balloon. HASP is supported by the NASA Balloon Program Office and the Louisiana Space Consortium, and has annual flights in September from the Columbia Scientific Balloon Facility (CSBF) base in Fort Sumner, New Mexico. HAXDT successfully completed its inaugural flight on September 1, 2012 with support from the Minnesota Space Grant Consortium. The discussion that follows describes the design of the HAXDT payload and the cosmic

ray detector, results from the 2012 flight, and planned upgrades for the next iteration of the payload. It should be noted that the detector design for the HASP flight described below detects energy levels insufficient for XNAV purposes ($>$ 300 keV) due to atmospheric absorption and electromagnetic interference, but the purpose of developing hardware to time the arrival of photon events is crucial to future XNAV flight opportunities. Therefore, the system described below is an important contribution to the XNAV community.

4.1 HAXDT Payload Systems and Principle of Operation

The twelve HASP payloads fall into two different classifications: there are four large class payload positions with an allowed footprint of 15 cm x 30 cm and a mass of up to 20 kg, and eight small class payload positions with an allowed footprint of 15 cm x 15 cm and a mass of up to 3 kg. The HAXDT payload is a small class payload with a measured mass of 1.5 kg and is designed to conform to CubeSat infrastructure standards, based on one or more cubes with internal dimensions of 10 cm x 10 cm x 10 cm. A single cube is known as a 1-U, or unit volume, configuration. The HAXDT payload is in a 2.5-U configuration with a footprint of 10 cm x 10 cm and a height of 25 cm as shown in Figure 4.1 below. The structure is composed of 6061-T6 aluminum and assembled using size 4-40 steel Socket Head Cap Screws. The hardware components are mounted to the exterior walls using custom standoff sizes. The CubeSat infrastructure allows the payload to be easily reconfigured to accommodate additional hardware components and future upgrades to X-ray detector hardware. The payload is ultimately being designed to test the system in space, thus the CubeSat model provides a flexible platform that can be modified for future space flight opportunities.

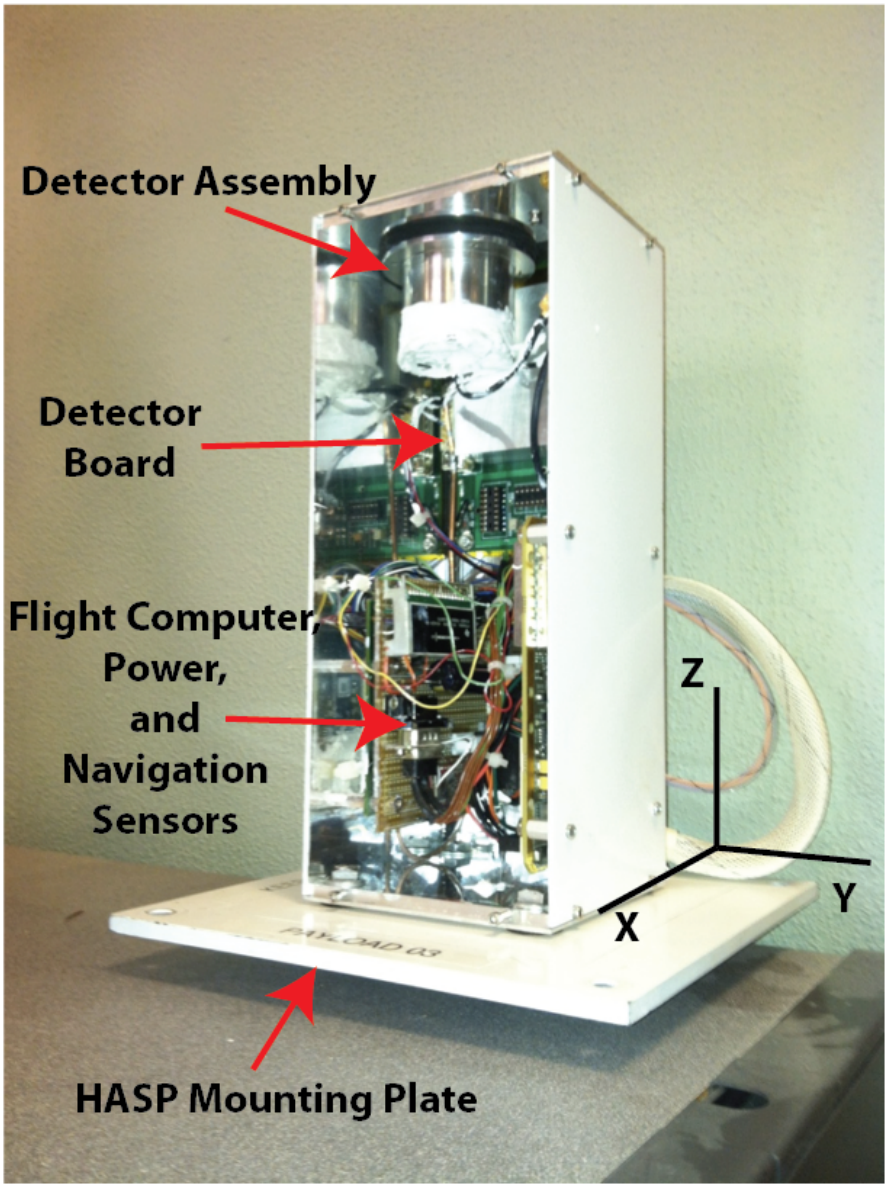

Figure 4.1: Open view of the HAXDT payload in a 2.5-U CubeSat configuration with a base of 10cm x 10cm and a height of 25cm. The payload is attached to the HASP mounting plate provided by the HASP program, and internal components are shown as labeled. The payload coordinate system is also indicated.

The HAXDT payload consists of a flight computer and daughter board, onboard flash storage, an inertial measurement unit (IMU), a GPS receiver, a power regulation and protection circuit, and a small detector capable of capturing high energy photon events and its associated hardware as described in the following section. The flight computer and attitude determination package has been developed by the Uninhabited Aerial Vehicle (UAV) Research Group at the University of Minnesota, and has a proven flight heritage [38]. The flight computer is a 32-bit PowerPC Phytec MPC5200B-tiny SoM. The MPC5200B has a clock frequency of 400 MHz and performs floating-point computation. This flight computer uses a real-time operating system written in C language, while a custom-designed daughter board handles the hardware interface to the flight computer. The flight code is open source code courtesy of the UAV Research Group at the University of Minnesota [38], and has been custom edited to perform attitude determination while collecting data from an X-ray detector. The GPS signal is provided using a Novatel OEMV-3G receiver modified for operation above 18 kilometers. The IMU is an Analog Devices ADIS16405 that provides angular rates and accelerations. Included on the device is a three-axis magnetometer and temperature sensor.

An attitude solution is obtained by combining the IMU data (rates, accelerations, and magnetic field) with the GPS position estimate. The data generated by the attitude determination system is placed in onboard storage through the flight computer for post processing. The detector data is also processed through the flight computer and stored as time-tagged photon events in the onboard flash storage.

4.2 Detector Design

Though X-ray detectors with large areas have been shown to provide acceptable navigation solutions for spacecraft [11, 15, 16], it has not been demonstrated that proposed smaller detectors provide such accuracies on long-term flights. Thus, smaller detectors

must be built and flown in order to gather valid data for analysis and algorithm development. Such detectors will have areas on the order of tens of square centimeters rather than square meters, and can be placed on any number of deep space mission spacecraft, including small vehicles such as CubeSats. The small X-ray detector design that is being studied consists of using an avalanche photodiode in combination with a scintillator. Although such a design may not be capable of detecting the low energy X-rays required for XNAV, it does allow a hardware system designed to count and store the photon time events used in XNAV to be flown and tested.

4.2.1 Avalanche Photodiode

Photomultiplier tubes are the most common light amplifiers used with scintillators [39]. However, a photodiode attached to scintillation material is also able to detect the flash of light that is generated by high-energy photons impacting the material. The photodiodes detection of this event creates an electrical pulse, which is equivalent to a high energy photon strike. This photon event is then counted by implementing an interrupt command on a microprocessor capable of high precision timing.

Photodiodes have several advantages over photomultiplier tubes such as compact size, durability, low power consumption, and the potential for better energy resolution due to higher quantum efficiency [39]. This efficiency is the ratio of the number of photoelectrons emitted to the number of incident photons. Thus, high quantum efficiency is essential in order to count as many photon strikes as possible.

An avalanche photodiode (APD) utilizes an internal gain that helps pull the signal up from the background electronic noise. This gain increases the small amount of charge that is otherwise produced in conventional photodiodes, thus providing better resolution for a scintillation event at lower radiation energy levels. APDs have a high breakdown voltage, thus a stable high voltage supply set to a suitable level below the breakdown

voltage must be applied. The gain is also affected by temperature, so the high voltage must be calibrated at the expected operational temperature to ensure proper resolution. It has been demonstrated that APDs used in conjunction with small volume scintillators have excellent energy resolution [39], thus affixing an APD to a small volume scintillator can function as a small cosmic ray detector.

4.2.2 Scintillator

The detection of ionizing radiation by the scintillation material should possess various attributes such as the ability to convert the kinetic energy of charged particles into detectable light, energy dispersion should attain as wide a range as possible, and a flash emitted by the material should decay quickly so as to create a detectable pulse of light [39]. Specific requirements for a scintillator used for XNAV include low energy resolution (X-ray energies of 0.1 to 10 keV), and very fast decay rates for high precision timing.

There are both organic and inorganic scintillator materials available. Inorganic scintillators have better light output, while organic scintillators are generally faster and yield less light [39]. Since fast timing is essential for X-ray navigation, a commercially available organic plastic material is an ideal choice to test and develop a small X-ray detector system. However, plastic scintillators experience significant degradation in light yield over time due to cumulative gamma ray exposure [39], which may inhibit their use on long duration spacecraft.

4.2.3 Detector Assembly

A simple detector consisting of an APD attached to scintillation material is both inexpensive and provides the means to test hardware designed to count energetic cosmic rays. The HAXDT payload provides a flexible platform both for testing the current

design and any future upgrades in detector capabilities, especially the detection of low energy X-rays. The current detector design is composed of an avalanche photodiode attached to an organic plastic scintillation material with optical grease. The detector is wrapped in polytetraflouroethylene (PTFE) tape and then seated in a 6061-T6 aluminum housing. It should be noted that the PTFE tape and aluminum housing provide limited shielding, thus the detector is assumed to be omnidirectional. An omnidirectional detector is not ideal for use in X-ray navigation, thus future designs must incorporate appropriate shielding so that the detector may be pointed at various X-ray sources. A picture of the detector design is shown below in Figure 4.2.

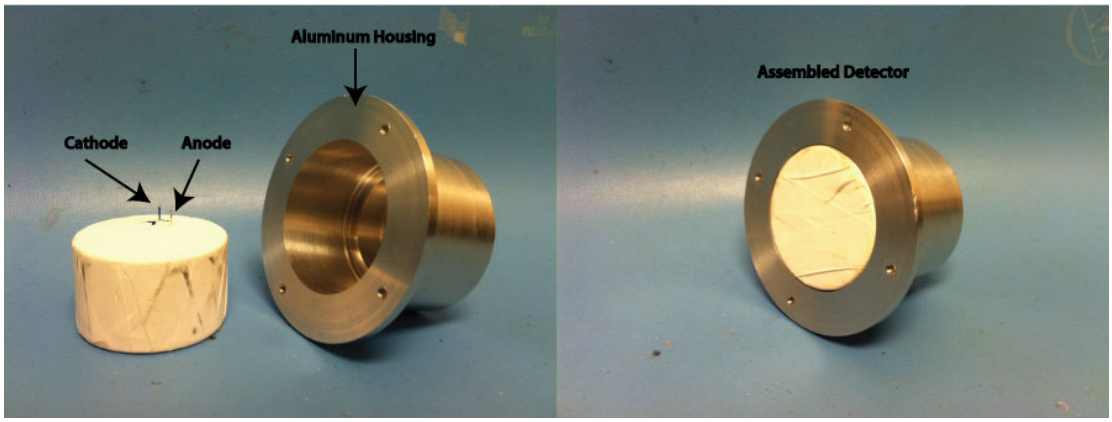

Figure 4.2: The HAXDT detector is comprised of an APD attached to a plastic scintillator and then wrapped in PTFE tape. Shown are the cathode and anode of the APD protruding from the PTFE tape (left). The wrapped assembly is then seated in the aluminum housing to complete the assembled detector (right).

The photodiode used within the system is a commercially available Hamamatsu silicon APD with an effective active area of 25 mm^2, a spectral response range between 320 and 1000 nm, and a typical breakdown voltage of 400 V. The scintillator material

is an organic plastic, BCF-12, from Saint-Gobain with a peak emission of 435 nm and decay time of 3.2 ns, thus the APD is capable of detecting scintillation events in the material. The APD is affixed to the scintillator material using a clear, colorless, silicone optical coupling compound from Saint-Gobain that features excellent light transmission. Lockheed Martin Space Systems Company's Advanced Technology Center has provided a front-end circuit board with a high voltage power supply and a single channel nuclear pulse-shaping circuit populated with an Amptek A225 preamp and A206 discriminator. This front-end board is capable of detecting single photon events generated by the APD/scintillator combination.

Laboratory testing of the design has shown that the system is capable of detecting cosmic rays above 300 keV after eliminating low-level noise, which is too high of an energy level to be used for X-ray navigation. Therefore, the design functions as expected, but must be revised for future flights to identify and remove these high energy events from processing and allow for resolution of low energy X-rays (0.1 - 10 keV) while withstanding sustained spaceflight operations.

4.3 HAXDT 2012 Flight Results

The 2012 HASP flight occurred on September 1, 2012, and launched from the CSBF base in Fort Sumner, NM. The HAXDT payload was operational for about 11.3 hours once power was provided during pre-launch operations. The flight system collected data throughout the entire flight, which included *Earth-Centered, Earth-Fixed* (ECEF) GPS position and velocity, IMU data (accelerations, rotational rates and magnetic field), internal ambient temperature, and scintillation event times. However, several lengthy GPS outages occurred during ascent with a maximum duration of about 1 hour. The cause of these outages is unknown, but it is suspected that the outages were due to extreme cold or electromagnetic interference. Thus, the GPS and IMU data provided a

semi-complete flight trajectory and attitude solution. The detector experienced no such outages and successfully collected scintillation events throughout the entire operation of the payload.

4.3.1 HAXDT Position and Attitude

Though some GPS data was lost during ascent, the NovAtel receiver functioned properly throughout the entire float portion of the flight, thus allowing a position solution to be determined for most of the flight. The ECEF position solution recorded by the GPS receiver was converted to the North-East-Down navigation reference frame and is shown below in Figure 4.3, where, again, gaps in the data indicate GPS outages that occurred during ascent to float altitude. Using the launch location as the starting reference position of $(East, North) = (0, 0)$, it was determined that the payload travelled approximately 780 km West and 70 km South with operations terminating west of Phoenix, AZ.

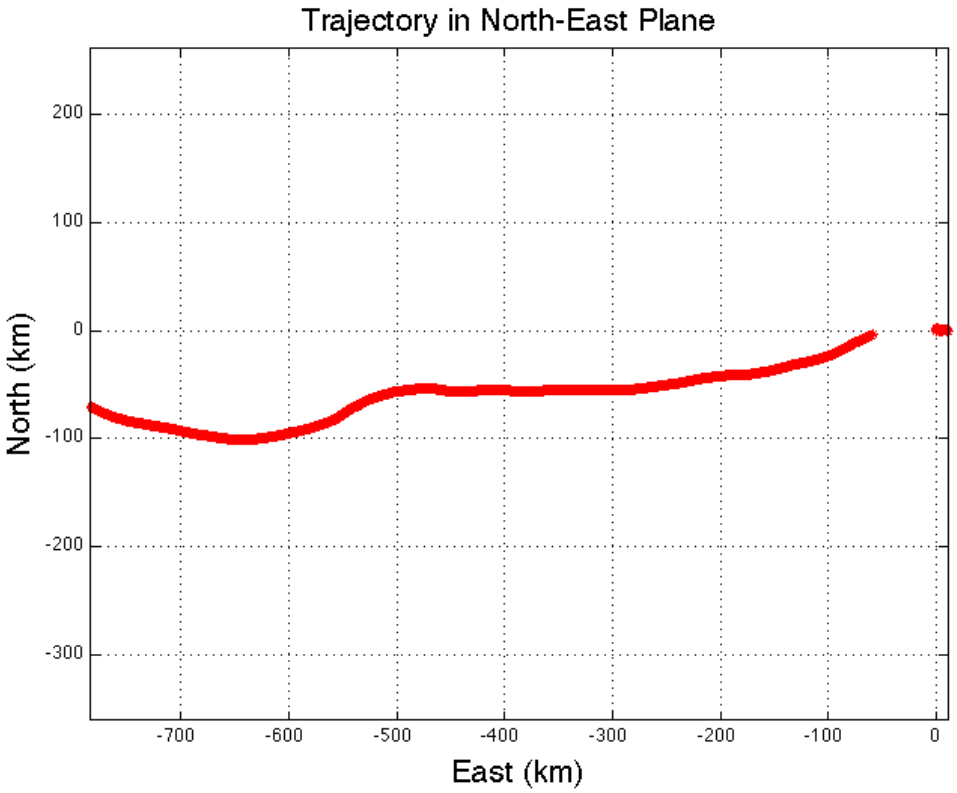

Figure 4.3: The North and East position of the HAXDT payload using the launch position as the (0,0) reference coordinate.

The attitude solution was found using a magnetometer-assisted Attitude and Heading Reference System (AHRS). The description of this method is outside the scope of this thesis, but it should be noted that it has been deemed an accurate solution by comparing the yaw solution to sections of video recorded during flight. As seen in Figure 4.3, the roll and pitch indicate a slight pendular motion, while the yaw indicates substantial rotational motion about the payload's Z-axis.

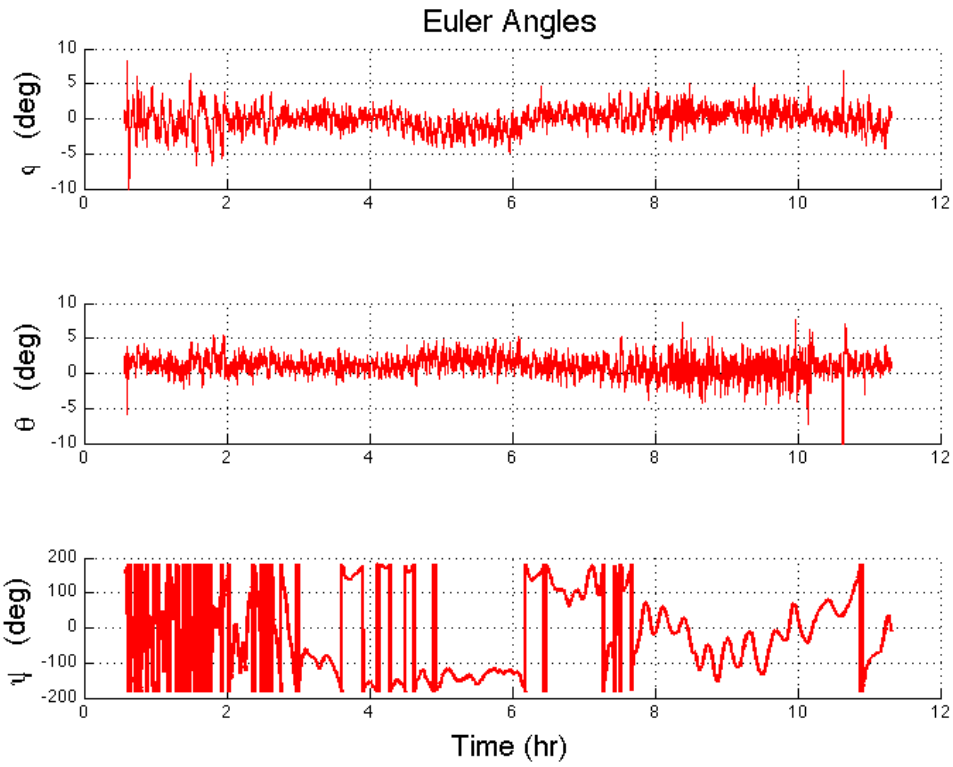

Figure 4.4: Time history of HAXDT payload Euler angle attitude solution showing roll (top), pitch (middle) and yaw (bottom).

The ability to successfully determine payload position and attitude is critical for locating celestial X-ray sources and pointing a detector at such sources. The HAXDT payload has successfully demonstrated that it is capable of providing these mission-critical requirements, but future improvements to the payload must ensure that no outages occur in order to maintain a complete navigation solution (position and attitude) throughout the entire flight.

4.3.2 HAXDT Detector Results

The detector successfully counted high-energy particle scintillation events, or photon events, for the entire time the HAXDT payload was operating, thus resulting in the collection of 1,115,740 photon events during operation as shown in Figure 4.5 below. Throughout the entire flight, the average photon count rate was 27.4 photons/sec, while the average photon count rate was 12.7 photons/sec after the HASP gondola reached float altitude.

As seen in Figure 4.5, there is a period of heightened activity during ascent, especially around 25km in altitude. This activity corresponds to an area in the atmosphere where cosmic rays initiate nuclear-electromagnetic cascades in the atmosphere, causing a maximum in secondary particle intensity. This area is called the *Pfotzer Maximum* and occurs at altitudes of 15-26 km depending on location and solar activity [40]. In comparing the altitude data to the recorded arrival rates in Figure 4.5, there is indeed a detected maximum level of particle intensity at 25km, and thus the drop in count rate for the duration of operations at float altitude is expected. However, the peak of this maximum is not resolved in the data due to poor budgeting of photon event storage in the HAXDT software. Therefore, the total average count rate as reported above do not entirely account for the intensity encountered in the Pfotzer maximum region. Also of note in Figure 4.5 is the internal ambient temperature profile as the payload ascends and operates at float altitude.

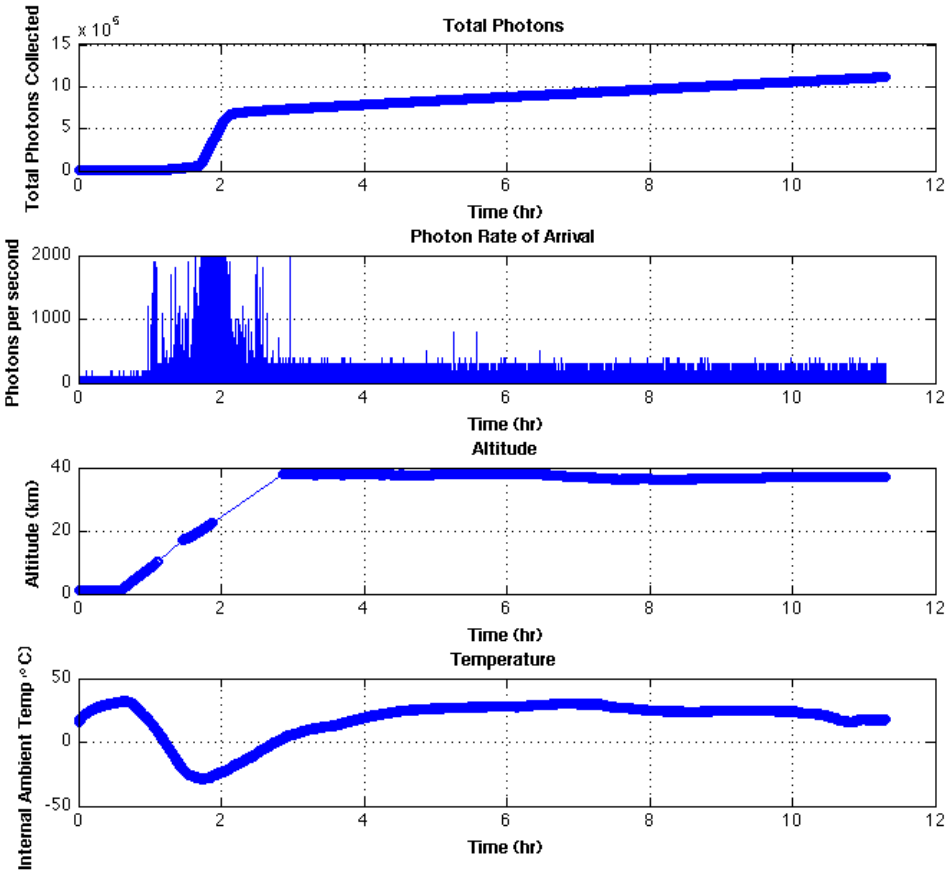

Figure 4.5: From top to bottom, plots of total number of photons collected, rate of photon arrival, altitude, and internal ambient temperature of the payload.

4.3.3 HAXDT Trajectory Transformation

The scientific objective of the HAXDT payload to build a detector capable of observing celestial sources requires the trajectory to be transformed to an inertial, or non-accelerating, celestial frame of reference. This is due to the fact that most known

celestial objects are charted in the geocentric *Right Ascension - Declination* (RA-Dec) frame of reference. Figure 4.6 below shows the RA-Dec frame, which is a right-handed inertial frame of reference defined by a vector that always points in the direction of the Earth's location at the vernal equinox and a vector that points in the direction of the North celestial pole. The RA-Dec frame is related to the geocentric *Earth-Centered Inertial* (ECI) frame of reference by the following:

$$\begin{bmatrix} X_{ECI} \\ Y_{ECI} \\ Z_{ECI} \end{bmatrix} = \begin{bmatrix} r\cos(\delta)\cos(\alpha) \\ r\cos(\delta)\sin(\alpha) \\ r\sin(\delta) \end{bmatrix} \tag{4.1}$$

where the Right-Ascension (α), Declination (δ), and the ECI coordinates X_{ECI}, Y_{ECI}, and Z_{ECI} are as shown in Figure 4.6, and r is the magnitude of the distance to some object plotted in the RA-Dec frame. It should be noted that the precise distance to celestial objects, or sources, are generally unknown, thus the unit direction to a celestial source is often used instead of an estimated distance.

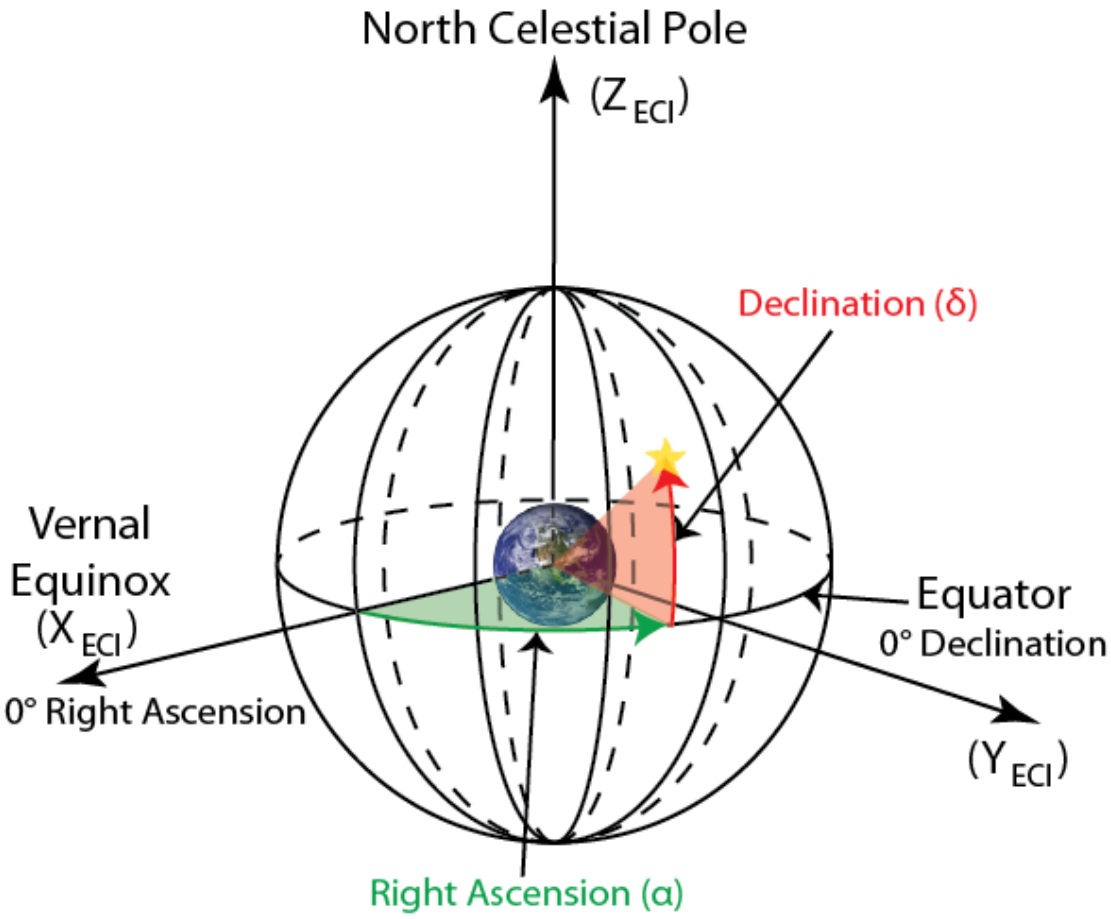

Figure 4.6: The Earth-centered inertial and geocentric right ascension - declination frames of reference.

As indicated in Equation 4.1, the ECEF coordinates collected by the GPS receiver must first be transformed to the ECI frame in order to obtain the RA-Dec coordinates of the HAXDT payload. The conversion from ECEF to ECI is non-trivial as it requires transforming time coordinates to celestial standards as well as the inclusion of other complex terms such as Earth's polar motion, precession, and nutation. One common

method used for the transformation from ECEF to ECI is the International Astronomical Union IAU-2000 Resolutions. A complete description of the IAU-2000 algorithm used to convert the HAXDT position coordinates can be found in [1]. Once the IAU-2000 transformation is applied, the ECI coordinates can be easily converted to RA-Dec using Equation 4.1.

The HAXDT position coordinates were transformed to the RA-Dec frame as described above and the resulting trajectory is shown in Figure 4.7 below. Because the roll and pitch motions as shown in Figure 4.4 were small, it is assumed that the detector onboard HAXDT was always pointing directly away from Earth. This assumption was used to plot a $\pm 15^{\circ}$ path to either side of the trajectory in order to simulate a detector with a 30° field of view as shown in Figure 4.7. Also shown in Figure 4.7 are various observations from two spacecraft, the Compton Gamma Ray Observatory (CGRO) and the International Gamma-Ray Astrophysics Laboratory (INTEGRAL). CGRO has an energy detection range of 30 keV to 30 GeV [41], while INTEGRAL has a range of 3 keV to 10 MeV [42], thus both spacecraft provide catalogs of sources that can be detected by the HAXDT payload. The catalogs used to plot the source observations from these spacecraft [43–46] can be found using NASA's High Energy Astrophysics Science Archive Research Center (HEASARC). These two spacecraft were chosen because the energy levels detected by the spacecraft are higher than the lowest energy the HAXDT payload is capable of detecting (>300 keV). As seen in Figure 4.7, the simulated detector encounters several celestial sources, including variable X-ray sources, thus indicating that the detector onboard HAXDT could possibly detect these sources on future flights when provided with proper shielding and the capability to determine energy levels of incident photons.

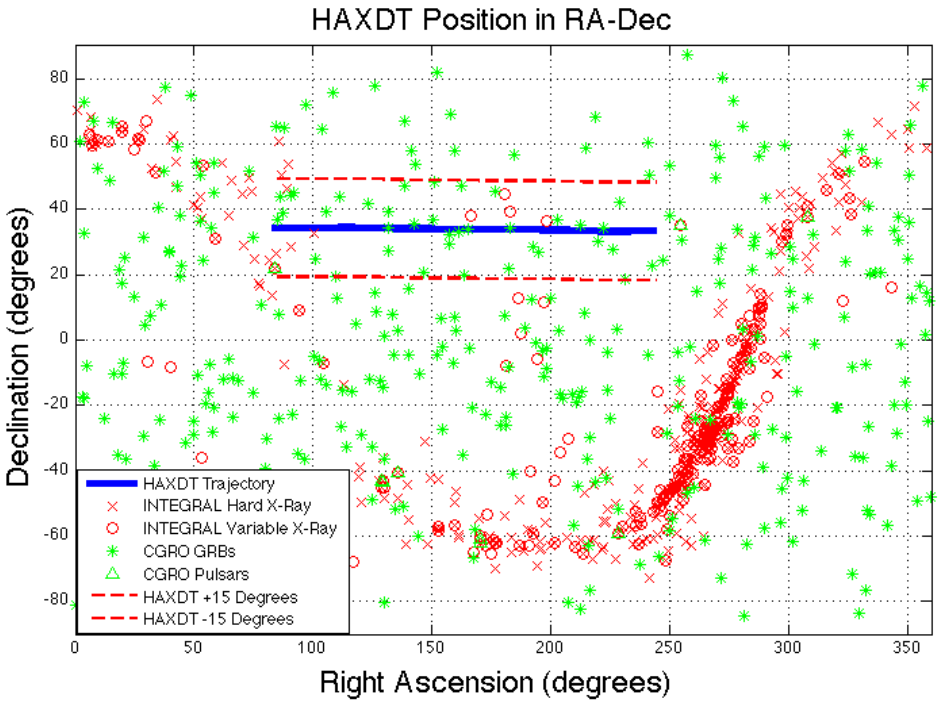

Figure 4.7: Trajectory of the HAXDT payload in the RA-Dec frame with a $\pm 15^{\circ}$ simulated field of view. Also shown are gamma-ray bursts and pulsars from the CGRO spacecraft (green data points) as well as hard and variable X-ray sources from the INTEGRAL spacecraft (red data points).

4.4 HAXDT Future Upgrades

The HAXDT payload has been awarded a second flight opportunity for the 2013 HASP flight. This flight is scheduled to launch September 2, 2013 from the CSBF base in Fort Sumner, NM. Currently, several upgrades of the HAXDT payload are under development for this next flight opportunity. The dimensions of the payload will be reconfigured to a 3-U CubeSat, thus providing more room for hardware upgrades including energy

resolution of detected photon events and temperature monitoring and control. The ability to resolve photon energies is important as it will allow the photon events to be interpreted as X-rays or gamma-rays, thus allowing photon events to be separated into different energy bands. Further, energy resolution will aid in the identification of specific celestial sources, which is critical when implementing XNAV algorithms. The detector shielding will also be improved by wrapping a sufficient volume of lead on the sides and bottom of the detector mount in order to narrow the region of the sky visible to the detector. Temperature monitoring and control will be added in order to minimize the suspected GPS data outages due to extreme cold. It is hoped that these upgrades will improve the performance of the navigation and attitude determination system as well as improve the omni-directionality of the detector system. It is anticipated that proper shielding and successful energy resolution will allow the HAXDT payload to identify celestial sources, thus bringing the payload closer to the ultimate goal of a fully functional X-ray navigation testbed.

Chapter 5

Conclusions

The primary goal of the research presented in this thesis was to investigate the use of small high-energy photon sensors for navigation applications. This involved proposing algorithms for the relative navigation of small spacecraft, developing a simulator system capable of modeling X-ray signals from celestial sources, and developing a hardware platform to test sensors and support the development of future XNAV algorithms. The discussion that follows includes an analysis of the results and technical contribution presented above and future work related to the work presented in this thesis.

5.1 Discussion of Simulation Results

A Matlab-based simulator capable of high-order timing of celestial X-ray sources was developed to fill the need for a tool to assist in analysis and algorithm development for X-ray based systems. This simulator is a valuable utility for testing algorithms such as the relative X-ray navigation algorithms presented in this thesis. The X-Ray Photon and Relativistic Effect Simulator System provides users with several options when implementing high-order time transfer equations. XPRESS simulation Modes B,

C, and D provide the nanosecond-level precision required for X-ray navigation while accounting for both geometric and relativistic effects. However, there are components of the time transfer equations that cause negligible effects that are included in Mode C and D that are not present in Mode B, such as the Proper Motion 2 and Römer 3 components defined in Table 3.1. Therefore, Mode B is the optimal choice for analysis and algorithm development when taking processing speed into account.

XPRESS is designed to simulate photon time events at the Solar System Barycenter. These time events are then processed through the time transfer equations as presented to simulate photon time events on a moving spacecraft. However, XPRESS does not require that the simulated photons occur at the SSB. This implies that XPRESS is a flexible platform that can test relative navigation algorithms by simulating photon arrivals at a spacecraft with a known absolute position with respect to the SSB (i.e. a Mother ship), and then transferring the photon time events to a spacecraft operating relative to the Mother ship (i.e. a Daughter ship). Therefore, XPRESS is a high fidelity simulator system that is capable of supporting many X-ray navigation concepts currently being studied, including those presented in this thesis.

5.2 Hardware Contribution

The High Altitude X-Ray Detector Testbed was developed to provide a platform for the testing of small X-ray detector hardware in a near-space environment. The HAXDT payload successfully completed its inaugural flight on September 1, 2012 onboard the High Altitude Student Platform. The small detector consisting of a plastic scintillator and avalanche photodiode successfully counted photon time events throughout the entire HASP flight. The avionics package provided payload trajectory and attitude information during the float portion of the flight, or at altitudes above 35 km, which is the flight profile of primary scientific interest. The payload is thus capable of providing

a trajectory in the Right Ascension - Declination celestial frame of reference while providing detector orientation information, both of which are required for celestial source identification. Therefore, the HAXDT payload is a suitable test bed for small X-ray detector hardware. However, there are several limitations that need to be addressed before future flight opportunities in order to extract celestial sources from the collected data.

5.3 Future Work

As presented in this thesis, XPRESS is a fully functional simulator that can be used to generate pulsar signals to test and verify XNAV algorithms. The algorithms presented in this thesis remain theoretical, so future testing and verification of these algorithms can utilize XPRESS to perform simulation studies. The addition of aperiodic source simulation would benefit such studies, so the addition of aperiodic examples is currently being explored to complement the current XPRESS configuration. Other upgrades currently being considered are adding a graphical user interface for ease of use, and providing portability to other languages such as C/C++.

Though the inaugural flight of the HAXDT payload was successful, there are several shortcomings that were encountered during the flight. The flight configuration of the detector lacked appropriate shielding, thus the detector was assumed to be omnidirectional. This inhibits the identification of celestial sources as the entire celestial sphere is essentially visible to the detector. In order to extract possible celestial sources, the detector must be shielded so that it can be pointed in a known direction along its trajectory. Additionally, the detector was unable to detect energy levels of photon time events. This feature would allow the detector to discriminate between X-ray and gamma ray sources, thus making source identification easier. The minimum detectable energy level was also too high for identification of X-ray pulsars used in X-ray navigation. This

threshold must be lowered if the payload is to provide a fully functional XNAV test bed.

In light of these limitations, upgrades to the detector hardware are currently in development for the second flight of the HAXDT payload, which is scheduled for September 1, 2013. These upgrades include detector shielding and energy resolution of the photon time events. Future flights will also seek to lower the energy threshold and add detector pointing capabilities.

5.4 Summary

The work in this thesis addresses the relatively unknown performance of small X-ray detectors through the development of a simulator system and hardware test bed. The simulator system provides a utility for future testing and verification of the presented algorithms, while the test bed provides a flexible platform that accommodates future upgrades in detector hardware and processing algorithms. These contributions successfully address the needs identified in this thesis, thus providing several useful tools for the advancement of X-ray based systems.

References

[1] David A. Vallado. *Fundamentals of Astrodynamics and Applications.* Microcosm Press, 3rd edition, 2007.

[2] Scott Gleason and Demoz Gebre-Egziabher. *GNSS Applications and Methods.* Artech House, 2009.

[3] Catherine L. Thornton and James S. Border. *Radiometric Tracking Techniques for Deep-Space Navigation*, volume 1 of *Deep Space Communications and Navigation Series.* Jet Propulsion Laboratory, 2000.

[4] Macgregor S. Reid. *Low-Noise Systems in the Deep Space Network*, volume 10 of *Deep Space Communications and Navigation Series.* Jet Propulsion Laboratory, 2008.

[5] Raymond A. Serway and Jr. John W. Jewett. *Physics for Scientists and Engineers.* Brooks/Cole - Thompson, 6th edition, 2004.

[6] D. J. Mudgway. *Uplink-Downlink, A History of the Deep Space Network 19571997.* National Aeronautics and Space Administration, 2001.

[7] Yanping Guo and Robert W. Farquhar. New horizons mission design. *Space Science Reviews*, 140(1-4):49–74, 2008.

[8] NASA. *New Horizons Mission Guide*. `http://pluto.jhuapl.edu`, 2006.

[9] Charles D. Edwards Jr, B. Arnold, R. DePaula, G. Kazz, C. Lee, and G. Noreen. Relay communications strategies for mars exploration through 2020. *Acta Astronautica*, 59(1):310–318, 2006.

[10] John E. Hanson. *Principles Of X-Ray Navigation*. PhD thesis, Stanford University, `http://search.proquest.com/docview/304316770/138003114322F6D6003/`, 1996.

[11] Suneel I. Sheikh. *The Use of Variable Celestial X-Ray Sources for Spacecraft Navigation*. PhD thesis, University of Maryland, `http://drum.lib.umd.edu/bitstream/1903/2856/1/umi-umd-2856.pdf`, 2005.

[12] D. W. Woodfork. The use of x-ray pulsars for aiding gps satellite orbit determination. Master's thesis, Air Force Institute of Technology, `http://www.dtic.mil/cgi-bin/GetTRDoc?AD=ADA437513`, 2005.

[13] S. I. Sheikh, D. J. Pines, K. S. Wood, P. S. Ray, M. N. Lovellette, and M. T. Wolff. Spacecraft navigation using x-ray pulsars. *Journal of Guidance, Control, and Dynamics*, 29(1):49–63, 2006.

[14] S. I. Sheikh and D. J. Pines. Recursive estimation of spacecraft position and velocity using x-ray pulsar time of arrival measurements. *Navigation: Journal of the Institute of Navigation*, 53(3):149–166, 2006.

[15] S. I. Sheikh, A. R. Golshan, and D. J. Pines. Absolute and relative position determination using variable celestial x-ray sources. In *Proc. AAS 30th Annual Guidance and Control Conference*, pages 1–20, 2007.

[16] S. I. Sheikh, P. S. Ray, K. Weiner, M. T. Wolff, and K. S. Wood. Relative navigation

of spacecraft utilizing bright, aperiodic celestial sources. In *Proc. ION 63rd Annual Meeting*, pages 444–453, 2007.

[17] A. R. Golshan and S. I. Sheikh. On pulse phase estimation and tracking of variable celestial x-ray sources. In *Proc. ION 63rd Annual Meeting*, pages 413–422, 2007.

[18] P. Graven, J. Collins, S. I. Sheikh, and J. E. Hanson. X-nav beyond the moon. In *Proc. ION 63rd Annual Meeting*, pages 423–431, 2007.

[19] P. S. Ray, S. I. Sheikh, P. H. Graven, M. T. Wolff, K. S. Wood, and K. C. Gendreau. Deep space navigation using celestial x-ray sources. In *Proc. ION 2008 National Technical Meeting*, pages 101–109, 2008.

[20] A. A. Emadzadeh. *Relative Navigation Between Two Spacecraft Using X-ray Pulsars*. PhD thesis, University of California, Los Angeles, `gradworks.umi.com/34/10/3410447.html`, 2009.

[21] S. I. Sheikh, J. E. Hanson, P. H. Graven, and D. J. Pines. Spacecraft navigation and timing using x-ray pulsars. *Navigation: Journal of the Institute of Navigation*, 58(2):165–186, 2011.

[22] P. Doyle, D. Gebre-Egziabher, and S. I. Sheikh. The use of small x-ray detectors for deep space relative navigation. In *Proc. of SPIE*, volume 8519, pages 85190K–1 – 85190K–12, 2012.

[23] Duncan Lorimer and Michael Kramer. *Handbook of Pulsar Astronomy*, volume 4 of *Cambride Observing Handbooks for Research Astronomers*. Cambridge University Press, 2005.

[24] Andrew Lyne and Francis Graham-Smith. *Pulsar Astronomy*, volume 48 of *Cambride Astrophysics Series*. Cambridge University Press, 4th edition, 2012.

[25] D. N. Matsakis, J. H. Taylor, and T. M. Eubanks. A statistic for describing pulsar and clock stabilities. *Astronomy and Astrophysics*, 326:924–928, 1997.

[26] Anders Brandt. *Noise and Vibration Analysis*. John Wiley & Sons, Inc., 2011.

[27] A. Possenti, R. Cerutti, M. Colpi, and S. Mereghetti. Re-examining the x-ray versus spin-down luminosity correlation of rotation powered pulsars. *Astronomy and Astrophysics*, 387:993–1002, 2002.

[28] L. Nicastro, G. Cusumano, O. Lhmer, M. Kramer, L. Kuiper, W. Hermsen, T. Mineo, and W. Becker. Bepposax observation of psr b1937+21. *Astronomy and Astrophysics*, 413:1065–1072, 2004.

[29] K. C. Gendreau. Next generation communications. Technical report, NASA Goddard Space Flight Center, `http://gsfctechnology.gsfc.nasa.gov/TechSheet/`, January 2012.

[30] P. Graven, J. Collins, S. Sheikh, J. Hanson, P. Ray, and K. Wood. Xnav for deep space navigation. In *Proc. AAS 31st Annual Guidance and Control Conference*, pages 1–16, 2008.

[31] S. I. Sheikh, J. E. Hanson, J. Collins, and P. Graven. Deep space navigation augmentation using variable celestial x-ray sources. In *Proc. ION 2009 International Technical Meeting*, pages 34–38, 2009.

[32] P. Misra and P. Enge. *Global Positioning System: Signals Measurements and Performance*. Ganja-Jamuna Press, 2006.

[33] P.J. de Jonge and C.C.J.M. Tiberius. Integer ambiguity estimation with the lambda method. In *Proc. IAG Symposium No. 115, GPS trends in precise terrestrial,*

airborne and spaceborne applications, XXI General Assembly of IUGG, pages 280–284, 1995.

[34] S. I. Sheikh, R. W. Hellings, and R. A. Matzner. High order pulsar timing for navigation. In *Proc. ION 63rd Annual Meeting*, pages 432–443, 2007.

[35] Jeffrey Schlosser. Random photon generator for xnav system using poisson processes. Internal CrossTrac Memorandum to Dr. John Hanson, July 2011.

[36] HEASARC. Observatories - swift. `http://heasarc.gsfc.nasa.gov/swift.html`. September 2013.

[37] NASA/JPL. Jpl horizons on-line ephemeris system. `ssd.jpl.nasa.gov/horizons.cgi`. May 2013.

[38] University of Minnesota Twin Cities UAV Research Group. Umn uav flight code. `www.uav.aem.umn.edu/`. April 2013.

[39] Glenn F. Knoll. *Radiation Detection and Measurement*. John Wiley & Sons, Inc., 4th edition, 2010.

[40] G.A. Bazilevskaya. Cosmic ray induced ion production in the atmosphere. *Space Science Reviews*, 137:149–173, 2008.

[41] HEASARC. Observatories - compton gamma-ray observatory. `http://heasarc.gsfc.nasa.gov/docs/cgro/cgro.html`. September 2013.

[42] HEASARC. Observatories - integral. `http://heasarc.gsfc.nasa.gov/docs/integral/integral.html`. September 2013.

[43] I. Telezhinsky, D. Eckert, V. Savchenko, A. Neronov, N. Produit, and T. J.-L. Courcoisier. The catalog of variable sources detected by integral. *Astronomy and Astrophysics*, 522(A68), 2010.

[44] R. Krivonos, S. Tsygankov, A. Lutovinov, M. Revnivtsev, E. Churazov, and R. Sunyaev. Integral/ibis nine-year galactic hard x-ray survey. *Astronomy and Astrophysics*, 545(A27), 2012.

[45] The BATSE GRB Team. The batse current gamma-ray burst catalog. `http://gammaray.msfc.nasa.gov/batse/grb/catalog/current`. Sept. 2001.

[46] HEASARC. Cgro/batse pulsar observations. `http://heasarc.gsfc.nasa.gov/W3Browse/cgro/batsepulsar.html`. March 2003.

Appendix A

Glossary and Acronyms

Care has been taken in this thesis to minimize the use of jargon and acronyms, but this cannot always be achieved. This appendix defines terms that are not variables that appear in *italics* throughout the thesis in a glossary, and contains a table of acronyms and their meaning.

A.1 Glossary

- **Absolute Navigation** – Position determination of a vehicle with respect to an inertial reference frame.
- **Corrected** – Photon time events that have been transferred from a spacecraft to the SSB by including geometric and relativistic effects.
- **Declination** – The angle between Earth's equatorial plane and to a location in the direction of the North celestial pole.
- **Deep Space** – The region of space near or above a geosynchronous Earth orbit.
- **Doppler Effect** – The observed change in frequency of a transmitted signal when

a source and receiver are moving relative to one another.

- **Earth-Centered, Earth-Fixed** (**ECEF**) – A rotating coordinate frame of reference that uses the center of the Earth as the origin with fixed axes at specific locations on the Earth's surface.

- **Earth-Centered Inertial** (**ECI**) – A right-handed inertial coordinate frame that uses the center of the Earth as the origin and is defined by a vector that always points towards the vernal equinox as the X-axis and the North celestial pole as the Z-axis.

- **Einstein Delay** – Pulsar timing delay due to gravitational redshift and time dilation.

- **Folding** – The synchronous averaging of a time series of collected photon events used to improve the SNR of the detected pulse through the addition of many pulses so that the signal is visible above the background noise.

- **Geosynchronous Earth Orbit** (**GEO**) – An earth-orbiting satellite with a period of 24 sidereal hours.

- **Gravitational Parameter** – The product of the gravitational constant, G, and the mass of a celestial body.

- **Hibernation Mode** – A spacecraft operational scenario in which most of the spacecraft is unpowered, or 'sleeping'.

- **Intertial Frame of Reference** – A non-acceletating frame of reference in constant rectilinear motion.

- **Lagrange Points** – Five positions in an orbital configuration where the combined gravitational pull of two large masses (e.g. the Earth and Moon) provides precisely

the centripetal force required to orbit with them.

- **Low Earth Orbit** (**LEO**) – An orbit about Earth up to 800 km in altitude above Earth's surface.
- **Pfotzer Maximum** – A region in the atmosphere at altitudes between 15 - 26 km where cosmic rays initiate nuclear-electromagnetic cascades, causing a maximum in secondary particle intensity
- **Proper Motion** – Radial and transverse motion of a source pulsar with respect to the Solar System barycenter.
- **Relative Navigation** – Position determination of a vehicle with respect to another vehicle or non-inertial (moving) reference frame.
- **Right Ascension** – The angle formed between a vector pointing towards the vernal equinox to a location on the Earth's equatorial plane.
- **Right Ascension - Declination** – A right-handed inertial coordinate frame that uses the center of the Earth as the origin and is defined by a vector that always points towards the vernal equinox as the and the North celestial pole and uses Right Ascension and Declination as position coordinates on the celestial sphere.
- **Römer Delay** – Pulsar timing delay incorporating classical geometry of the Solar System including the effect of wavefront curvature.
- **Round-Trip Light Time** (**RTLT**) – The time it takes for a radio signal generated at an Earth-based station to reach a spacecraft and be transmitted back to Earth.
- **Semi-synchronous Orbit** – An earth-orbiting satellite with a period of 12 sidereal hours.

- **Shapiro Delay** – Pulsar timing delay due to the curvature of spacetime caused by masses present in the Solar System.
- **Signal-to-Noise Ratio** (**SNR**) – A measure that compares the level of a desired signal to the level of background noise.
- **Solar System Barycenter** (**SSB**) – The center of mass of the solar system that serves as an inertial reference frame for celestial X-ray source observations.
- **Time-of-Arrival** (**TOA**) – The arrival time of some fiducial point of interest such as the peak of a pulse.
- **Uncorrected** – Photon time events that occur at a detector on a spacecraft and exclude geometric and relativistic effects.

A.2 Acronyms

Table A.1: Acronyms

Acronym	**Meaning**
AHRS	Attitude and Heading Reference System
APD	Avalanche Photodiode
CGRO	Compton Gamma Ray Observatory
CSBF	Columbia Scientific Balloon Facility
DARPA	Defense Advanced Research Program Agency
DSN	Deep Space Network
ECEF	Earth-Centered, Earth-Fixed
ECI	Earth-Centered Inertial

Continued on next page

Table A.1 – continued from previous page

Acronym	**Meaning**
ESA	European Space Agency
GEO	Geosynchronous Earth Orbit
GNSS	Global Navigation Satellite System
GPS	Global Positioning System
HASP	High Altitude Student Platform
HAXDT	High Altitude X-ray Detector Testbed
HEASARC	High Energy Astrophysics Science Archive Research Center
IMU	Inertial Measurement Unit
INTEGRAL	International Gamma-Ray Astrophysics Laboratory
JPL	Jet Propulsion Laboratory
LEO	Low Earth Orbit
MRO	Mars Reconnaissance Orbiter
NASA	National Aeronautics and Space Administration
PTFE	Polytetraflouroethylene
RA-Dec	Right Ascension - Declination
RTLT	Round-Trip Light Time
SNR	Signal-to-Noise Ratio
SSB	Solar System Barycenter
TOA	Time-of-Arrival
UAV	Uninhabited Aerial Vehicle
XNAV	X-ray Source-based Navigation for Autonomous Position Determination
XPRESS	X-ray Photon and Relativistic Effect Simulator System